INITIAL CONDITIONS FROM COLOR GLASS CONDENSATE

A Dissertation

by

GUANGYAO CHEN

Submitted to the Office of Graduate Studies of
Texas A&M University
in partial fulfillment of the requirements for the degree of

DOCTOR OF PHILOSOPHY

Chair of Committee,	Rainer J. Fries
Co-Chair of Committee,	Che-Ming Ko
Committee Members,	Saskia Mioduszewski
	Joseph B. Natowitz
Head of Department,	George R. Welch

August 2013

Major Subject: Physics

ABSTRACT

Nuclei at very high energy, characterized by a saturation scale, can be described by an effective theory of Quantum ChromoDynamics (QCD) called Color Glass Condensates. The earliest phase of the collision of two nuclei is modeled as the collision of two sheets of color glass. The classical field resulting from the collision then decays and equilibrates to a plasma of quarks and gluons. Using a recursive solution of the Yang-Mills equations, we calculate analytic expressions for the gluon field created in ultra-relativistic heavy ion collisions at small times τ. We have worked out explicit solutions for the fields and the energy momentum tensor up to 4^{th} order in an expansion in τ. We generalize the existing calculations to go beyond the limit of large homogenous nuclei. This allows us to calculate radial and elliptic flow of gluon fields. The resulting transverse and longitudinal structure of the Poynting vector field has a rich phenomenology. Besides the well known radial and elliptic flow in transverse direction, classical quantum chromodynamics predicts a rapidity-odd transverse flow that tilts the fireball for non-central collisions, and it implies a characteristic flow pattern for collisions of non-symmetric systems $A + B$. The rapidity-odd transverse flow translates into a directed particle flow v_1 which has been observed at RHIC and LHC. The global flow fields in heavy ion collisions could be a powerful check for the validity of classical Yang-Mill dynamics in high energy collisions. We also propose a procedure to calculate the energy momentum tensor of gluon fields on an event-by-event basis. The matching of the initial field energy momentum tensor to viscous hydrodynamic initial conditions is discussed and some preliminary results of a subsequent hydrodynamic evolution are shown. Our results can provide event-by-event initial conditions for hydrodynamic simulations of nuclear collisions that

include initial flow and initial shear stress.

DEDICATION

To my family.

ACKNOWLEDGEMENTS

First, I would like to thank my advisor, Prof. Rainer J. Fries, for his guidance. I might not have finished my Ph.D. without his encouragement and help. His insights are critical to my research.

I wish to express my gratitude to Prof. Che-Ming Ko, Prof. Saskia Mioduszewski and Prof. Joseph B. Natowitz for their service in my dissertation committee and for their help during my graduate study. I thank Dr. Aldo Bonasera for attending my final exam.

I also thank my M.S. advisor, Prof. Jue-ping Liu, for his earlier education and training. I acknowledge discussions with Dr. Ricardo Rodriguez, Dr. Xingbo Zhao, Dr. Min He, Prof. Ralf Rapp, Feng Li, Hua Zheng. I also want to thank Sidharth Somanathan for collaboration.

Last but not least, I would like to thank my parents, my sisters and especially my wife, Yanyi Li. I am especially indebted for Yanyi's patient and understanding during my graduate study.

TABLE OF CONTENTS

LIST OF FIGURES

FIGURE Page

1. INTRODUCTION

Quantum ChromoDynamics (QCD) has been used to describe the interactions of quarks and gluons very successfully. When momentum transfers are large, the perturbative QCD (pQCD) is applicable due to asymptotic freedom [1, 2]. Lattice QCD (lQCD) (for a recent review, see e.g. [3]) predicts that protons and neutrons will melt into a deconfined phase called Quark Gluon Plasma (QGP) [4, 5] which exists above a pseudo critical temperature $T_c \sim 150 - 160$ MeV [6, 7]. The experiments at the Relativistic Heavy Ion Collider (RHIC) and Large Hadron Collider (LHC) provide physicists opportunities to explore matter under conditions of such extreme density and pressure. Matter under those extreme conditions is of interest for several reasons. Firstly, we can explore properties of QCD in the non-perturbative regime, e.g. the structure of the phase diagram; secondly, QGP is believed to be relevant for the earliest phase of the universe $\sim (10^{-5}$ s); furthermore, some high density astrophysical objects, like neutron stars, are speculated to be made of dense quark matter. Here we are mostly interested in the QGP, and the best way to create and study it in the laboratory is through ultra-relativistic heavy-ion collisions (URHICs).

1.1 Quantum ChromoDynamics

The classical Lagrangian density of QCD has quark and gluon fields as its fundamental degrees of freedom. For a quark of mass m_f according to its flavor f, the Lagrangian can be written as,

$$\mathcal{L}_{cl} = \sum_{f}^{N_f} \bar{q}_f (i\gamma^\mu D_\mu - m_f) q_f - \frac{1}{4} F_a^{\mu\nu} F_{\mu\nu}^a \,. \tag{1.1}$$

D_μ is a covariant derivative which acts on colored quark fields q_f ($f = u, d, s, c, b, t$),

$$D_\mu = \partial_\mu - igt^a A^a_\mu \,, \tag{1.2}$$

where A^a_μ is the gluon field and t^a, $a = 1, ..., 8$, are 3×3 traceless hermitian matrices which are a fundamental representation of the $\mathrm{SU}(3)_c$ Lie algebra satisfying

$$[t_a, t_b] = i f_{abc} t_c \ , \tag{1.3}$$

with f_{abc} being the structure constants of $\mathrm{SU}(3)_c$.

The field strength tensor $F^a_{\mu\nu}$ of gluons is given by

$$F^a_{\mu\nu} = \partial_\mu A^a_\nu - \partial_\nu A^a_\mu + ig f_{abc} A^b_\mu A^c_\nu \ , \tag{1.4}$$

in terms of the gluon gauge fields A^a_μ ($a = 1 \cdots 8$).

QCD has several properties that make it very intriguing and complicated. The first fascinating property of QCD is the *asymptotic freedom* of the coupling constant $\alpha_s = g^2/4\pi$. Unlike in QED, where only fermions carry charges, in QCD quarks *and* gauge boson – the gluons – carry color charge. This is explicitly shown by the last term in Eq. (1.4) which leads to interactions between gluons. Consequently the coupling constant of QCD α_s decreases logarithmically as the momentum transfer increases [1, 2, 8],

$$\alpha_s(Q) = \frac{g^2}{4\pi} = \frac{1}{\beta_0 \ln(Q^2/\Lambda^2_{QCD})} \,, \tag{1.5}$$

where $\beta_0 = (33 - 2n_f)/(12\pi)$ for QCD. If the momentum transfer Q is smaller than the scale $\Lambda_{QCD} \simeq 200$ MeV, $\alpha_s(Q)$ formally diverges. However Eq. (1.5) is obtained

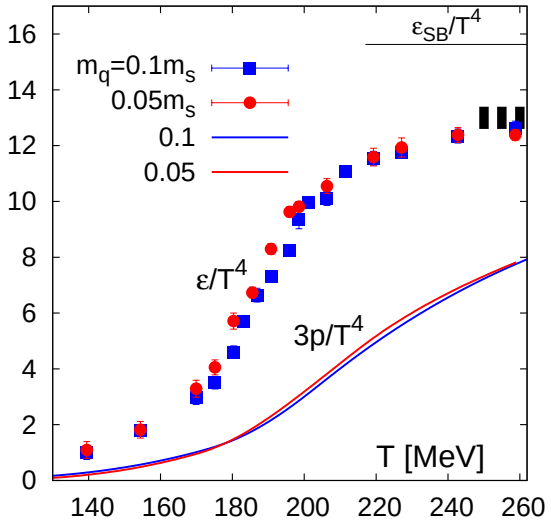

Figure 1.1: Energy density over temperature to the fourth order (T^4) and three times the pressure over T^4 for physical light quark mass and $m_l = 0.1m_s$. Reprinted figure with permission from M. Cheng et. al, Phys. Rev. D 81, 054504 (2010) [9]. Copyright (2010) by the American Physical Society.

from perturbative calculations and is not strictly applicable for small Q. In the "perturbative" regime with large momentum transfer $Q \gg 1\,\mathrm{GeV}$, theoretical predictions have been tested up to very high precision by various experiments. However, perturbative calculations break down already at momentum transfers well above Λ_{QCD}. If the momentum transfer is not significantly greater than Λ_{QCD}, "non-perturbative" techniques are required for QCD calculations.

Another intriguing property of QCD is *confinement*, which refers to the fact that colored charged particles, e.g. quarks and gluons, cannot be isolated singularly, and as a result we cannot directly observe a colored object. Nevertheless, the fact that quarks carry three different color charges has been confirmed by experiments without

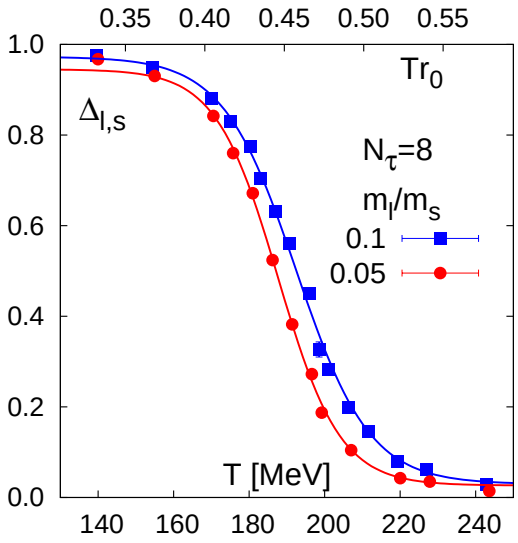

Figure 1.2: The subtracted chiral condensate as function of the temperature calculated at $m_l = 0.05m_s$ and at $0.1m_s$. Reprinted figure with permission from M. Cheng et. al, Phys. Rev. D 81, 054504 (2010) [9]. Copyright (2010) by the American Physical Society.

a doubt. Heavy Ion Collisions give physicists opportunities to study the properties of quarks and gluons in the deconfined phase at high temperature. Fig. 1.1 shows the theoretical predictions from lattice QCD. The energy density of nuclear matter increases rapidly at $T \sim 180 - 200$ MeV, indicating a large jump in the number of degrees of freedom when going from a hadronic gas to QGP.

One more very interesting phenomenon in QCD related to the QCD phase transition is *chiral symmetry breaking*. In the chiral limit where the light quark mass is negligible $m_u, m_d \to 0$, the QCD Lagrangian can be approximated as,

$$\mathcal{L}_{chiral} = \sum_{l=u,d} \bar{q}_l (i\gamma^\mu D_\mu) q_l - \frac{1}{4} F_a^{\mu\nu} F^a_{\mu\nu} \ . \tag{1.6}$$

We define the left- and right-handed projector for quarks as $P_L = \frac{1}{2}(1-\gamma^5)$ and $P_R = \frac{1}{2}(1-\gamma^5)$), respectively, where $\gamma^5 = i\gamma^0\gamma^1\gamma^2\gamma^3$. We can decompose the quark field $q = (u,d)^T$ into its chiral components,

$$q_L = P_L q, \qquad q_R = P_R q\,. \tag{1.7}$$

Eq. (1.6) then can be written as,

$$\mathcal{L}_{chiral} = \bar{q_L}(i\gamma^\mu D_\mu)q_L + \bar{q_R}(i\gamma^\mu D_\mu)q_R - \frac{1}{4}F_a^{\mu\nu}F^a_{\mu\nu}\ , \tag{1.8}$$

and in the chiral limit the Lagrangian exhibits chiral symmetry, i.e. it is symmetric under rotation in flavor space for each chirality. However, because of the nontrivial structure of QCD vacuum, there is a non-vanishing expectation value

$$\langle\bar{q}q\rangle = \langle\bar{q}_R q_L + q_L q_R\rangle \approx \Lambda^3_{QCD}\,. \tag{1.9}$$

Quarks interacting with this condensate will acquire an effective mass about 300 MeV. The chiral symmetry is spontaneously broken for hadrons and it turns out that the melting of chiral condensate and the restoration of chiral symmetry take place around the same pseudo-critical temperature that matters became deconfined. Fig. 1.2 shows the melting of chiral condensate predicted by lQCD [9, 10].

The above features of QCD can be summarized in a QCD phase diagram, see Fig. 1.3. When both temperature and density are low, nuclear matter lives in a hadronic phase with spontaneously broken chiral symmetry. The deconfined quark-gluon phase exists at high temperature. Various forms of quark Cooper pairing in the domain of high-density but low-temperature will give rise toColor-SuperConducting (CSC) phases. The dashed line illustrates the chiral crossover transition predict by

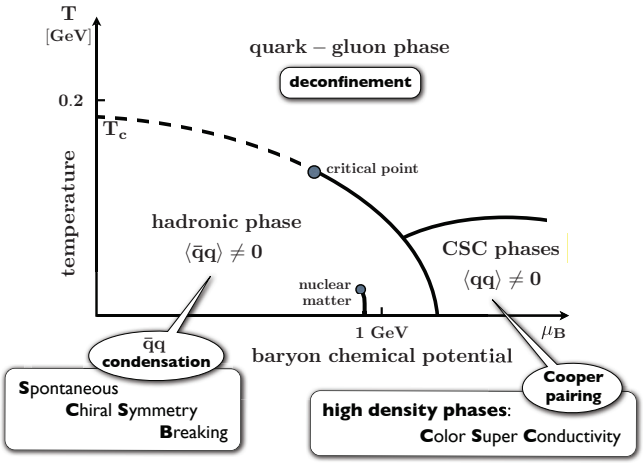

Figure 1.3: Schematic picture of the QCD phase diagram with respect to temperature T and baryon chemical potential μ_B. Figure reprinted from [11] with permission from ELSEVIER.

lQCD. Currently it is believed that the crossover will end at a hypothetical critical point where a first-order phase transition (solid line) begins. Physicists at RHIC are actively searching for the critical point at this time [12].

1.2 Relativistic Heavy Ion Collisions

There is convincing evidence that the QGP has been created in the laboratory through heavy ion collision at RHIC [4, 5] and LHC [13, 14, 15]. The Relativistic Heavy Ion Collider located at Brookheaven National Laboratory (BNL) is built to collide nuclei at center of mass (c.m.) energy up to $\sqrt{s_{NN}} = 200$ GeV per nucleon pair. The Large Hadron Collider is located at the European Organization for Nuclear Research (CERN), and the colliding energy of the nucleon pair can reach 5.5 TeV for large nuclei.

The idea of a heavy ion collider is that a large amount of energy will be deposited into a very small spatial region by accelerating heavy nuclei to ultra-relativistic speed and colliding them. A large amount of the kinetic energy will be converted to thermal energy in a very short time scale (less than 100 fm /c $\sim 10^{-22}$ s) resulting in extremely high density and temperature. The top energy density created at RHIC is estimated to be larger than 15 GeV / fm^3 [4, 5], and the top energy density created at LHC is estimated to be about 3 times larger [16].

Some of important experimental signatures of QGP can be summarized below [4, 5]:

1. Signatures from the phase transition. New degrees of freedom by deconfining quarks and gluons at sufficiently high temperature will result in a rapid increase in energy density ϵ, entropy density s and pressure p around the critical temperature, see Fig. 1.1. The drastic change in the number of degrees of freedom will be reflected in various final observables, such as the hadron multiplicity dN/dy, the transverse energy $dE_\perp/dy$, and the average transverse momentum $\langle p_\perp \rangle$, the collective behaviors and so on. Hydrodynamics and statistical models are useful tools to explore these signatures.

2. Jet Quenching and Parton Energy Loss. Bjorken firstly pointed out that partons traveling through bulk partonic matter might undergo significant energy loss [18], which is can be observed by measuring subsequent hadrons of the parton from fragmentation. More quantitative theoretical calculations showed that gluon radiation induced by passage through the matter is significant [19] and such induced gluon radiation would soften and broaden the jets. The suppression and broadening of jets has been confirmed by experimental data [20].

3. Quark Recombination. Recombination models [21, 22, 23, 24, 25] were introduced to explain observed features of hadron production RHIC collisions. The recombination models predict effects on baryon and meson production rates [26, 27] by assuming that coalescence proceeds via *constituent* quarks. Recombination models are able to explain the key properties of final particles observed in experiments like elliptic flow [28], and allow a conclusion that such properties are formed in the deconfined phase.

4. Electromagnetic Probes. Due to the fact that photons and dileptons only interact electromagnetically with the surrounding matter, the mean free path of photons and dileptons is much larger than the typical size of the hot quark matter created by heavy ion collisions. As a result photons and dileptons can provide undisturbed information inside the fireball, e.g. about the temperature of the QGP. For recent review see [29].

5. Heavy quarks. It had first been pointed out by Matsui and Satz that the J/ψ yield should be suppressed in URHIC if QGP is created. Due to the color Debye screening, the binding potential becomes short-ranged [31, 32].

The space-time picture of a heavy ion collision (HIC) is sketched in Fig. 1.4. This depicts the quark matter during various stages after the collision which we will discuss now:

1. Preceding the collision, the two incoming nuclei can be described as two Lorentz–contracted 'pancakes' in the laboratory frame. The Lorentz–contraction factor is about 100 for RHIC and 3500 for LHC. The wavefunction of such a high energy nucleus is dominated by *gluons* which carry small fractions of the longitudinal momenta of their parent nucleons, or more precisely, gluons with

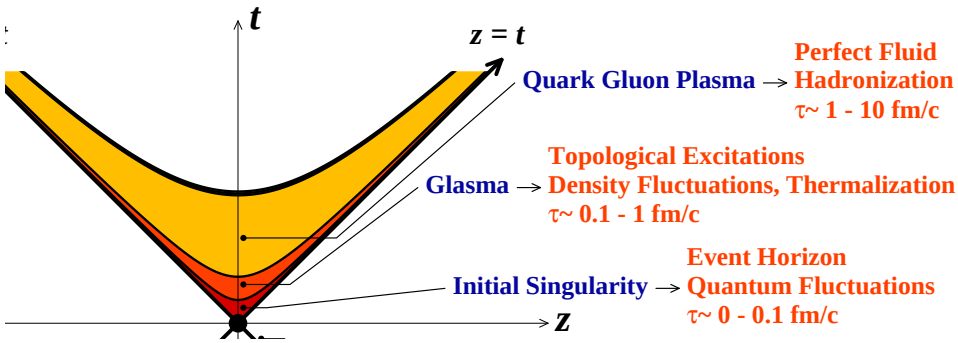

Figure 1.4: Schematic space-time picture of a HIC as a function of time t and the longitudinal coordinate z along the beam axis. Figure reprinted from [33] with permission from the author.

Bjorken-$x \ll 1$. From measurement of parton distribution functions, we learn that the density of small x gluons $xg(x, Q^2)$ increase rapidly at small x until gluon fusion ($g+g \to g$) is as important as gluon splitting ($g \to g+g$) processes, characterized by a saturation scale Q_s. From the uncertainty principle, such high density gluons should carry large transverse momentum. For example, the transverse momentum $k_\perp$ is roughly 2 GeV for a gluon with $x = 10^{-4}$ [33]. The coupling constant in this regime with large scale Q_s should be relatively small because of asymptotic freedom. An effective theory of QCD called the Color Glass Condensate (CGC) [36, 37] has been written down to describe such nuclei at very high energy and large occupation number.

2. Two nuclei moving with the speed of light hit each other at time $\tau = 0$, where τ is the longitudinal proper time. From the uncertainty principal, the time scale of an interaction is proportional to the inverse of the momentum transfer

$1/Q$. Hard probes, i.e. particles with very high momentum $Q \gg 1$ GeV, are produced very fast after the two nuclei collide. From the CGC perspective, the gluon fields in the initial incoming nuclei are liberated through the collisions and the subsequent dynamics of their interaction and evolution of the matter, so called Glasma, are governed by the Yang-Mills equations up to a time scale $\tau \sim 1/Q_s$. Where Q_s is the saturation scale which characterize the scale which parton density stops growing rapidly as x decreases. The value of Q_s is about 1 GeV at RHIC and $Q_s \sim 4$ GeV at LHC [38, 39]. Here, we are particularly interested in the evolution of such early time energy momentum tensor of the glasma.

3. The classical Yang-Mills equations do not predict thermalization. However, experimental data from both RHIC and LHC suggest a rapid thermalization of the bulk matters produced in heavy ion collisions. The data, when compared to hydrodynamic models, are consistent with a relatively short thermalization time, of order $\tau \sim 1$ fm/c for RHIC [40] and thermalization time at LHC is estimated to be even shorter than at RHIC but quantitative study is not available yet. The microscopic understanding of equilibration requires a more complete description of quantum non-abelian dynamics [41, 42, 43], and it is outside the scope of this dissertation.

4. The thermalized, deconfined and strongly interacting phase of QCD matter called the quark gluon plasma exists roughly for about $\tau \sim 10$ fm/c after the collision happened. The properties of strongly interacting matter enable us to depict its evolution using the relativistic hydrodynamics. We will introduce the basic concepts of hydrodynamics in the next section.

5. As the hot and dense system is expanding, the temperature decreases. When

the critical temperature ($T_c \sim 150-160$) is reached, the deconfined quark-gluon plasma undergoes a transition to a hadronic matter. The hadronic matter still maintains approximately local thermal equilibrium, and hydrodynamics can still characterize the evolution of the hot hadronic gas until kinetic freeze out temperature around 100 MeV is reached. There is also work to study the dynamics of the hadronic phase with transport models like Ultrarelativistic Quantum Molecular Dynamics model (URQMD) [44].

1.3 Relativistic Hydrodynamics

The utilization of hydrodynamics in nuclear collision was first proposed by Landau [45] and successfully applied by Bjorken [46]. For a review please refer to [47, 48]. The general form of the energy-momentum tensor of an ideal relativistic fluid can be written as,

$$T^{\mu\nu}_{ideal} = e\ u^\mu u^\nu - p\ \Delta^{\mu\nu} \tag{1.10}$$

where $\Delta^{\mu\nu} = g^{\mu\nu} - u^\mu u^\nu$ is a operator orthogonal to the fluid velocity u^μ, and e and p are energy density and pressure, respectively, in the local rest frame of the fluid. If there are no external sources, as for the QGP created by HICs, the energy momentum tensor should be conserved and satisfy

$$\partial_\mu T^{\mu\nu}_{ideal} = 0\,. \tag{1.11}$$

If there are conserved charges, like net baryon number, we also should have conservation of the corresponding current j^μ,

$$\partial_\mu j^\mu = 0\,. \tag{1.12}$$

Equation (1.10) can be written in terms of scalar quantities,

$$u^\mu \partial_\mu e + (e+p)\partial_\mu u^\mu = 0 \tag{1.13}$$

$$(e+p)u^\mu \partial_\mu u^\alpha - \Delta^{\mu\alpha}\partial_\mu p = 0 \ . \tag{1.14}$$

These equation will reduce to the non-relativistic hydrodynamic equations for $|\vec{v}| \ll 1$.

If dissipative effects are to be included, the energy momentum tensor of the fluid will have additional terms to Eq. (1.10) and can be written as

$$T^{\mu\nu} = T^{\mu\nu}_{ideal} + \Pi^{\mu\nu}, \tag{1.15}$$

where $\Pi^{\mu\nu}$ is the viscous stress tensor which describes deviations from local thermal equilibrium. It is conventional to decompose $\Pi^{\mu\nu}$ to a traceless part $\pi^{\mu\nu}$ and its reminder $\Delta^{\mu\nu}\Pi$. The shear viscous stress tensor must be orthogonal to the fluid velocity $u_\mu \pi^{\mu\nu} = 0$.

The fundamental conservation equations then read,

$$\begin{aligned} u^\mu \partial_\mu e + (e+p)\partial_\mu u^\mu - \Pi^{\mu\nu}\nabla_{(\mu}u_{\nu)} &= 0 \,, \\ (e+p)u^\mu \partial_\mu u^\alpha - \Delta^{\mu\alpha}\partial_\mu p + \Delta^\alpha_\nu \partial_\mu \Pi^{\mu\nu} &= 0 \ . \end{aligned} \tag{1.16}$$

where $A_{(\mu}B_{\nu)}$ is short notation for symmetrization $A_{(\mu}B_{\nu)} = \frac{1}{2}(A_\mu B_\nu + A_\nu B_{\mu)})$.

In addition, one has to postulate equations for $\Pi^{\mu\nu}$. In first-order viscous hydrodynamics they are given by gradients of the velocity field times the viscosity,

$$\pi^{\mu\nu} = \eta \nabla^{<\mu} u^{\nu>} \,, \quad \Pi = \zeta \nabla_\alpha u^\alpha \,, \quad \eta \geq 0 \,, \quad \zeta \geq 0 \,, \tag{1.17}$$

where η is the shear viscosity and ζ the bulk viscosity coefficient, and $A_{<\mu}B_{\nu>}$is the traceless part of $A_{(\mu}B_{\nu)}$. Eq.(1.17) is called the Navier-Stokes approximation. The Navier-Stokes approximation does not preserve causality. Consequently various second order viscous hydrodynamic models were introduced. For example, the Muller-Israel-Stewart theory [49, 50], and others [51, 52]. For a recent review of viscous hydrodynamics refer to [53, 54].

These hydrodynamic equations together with an Equation of State (EOS) can predict the long wavelength behavior of a fluid with given initial conditions.

The most convincing evidence that thermalized QPG is produced in heavy ion collisions comes from the hydrodynamic behavior of transverse momentum distribution and collective flow of final particles. The $m_\perp$ scaling

$$E\frac{d^3N}{d^3p} \approx exp(-m_\perp/T) \tag{1.18}$$

observed in URHIC for particle with $p_\perp < 2$ is a strong evidence that a thermal equilibrium matter has been created in URHIC. The azimuthal momentum distribution of final particles can be expanded into a Fourier series,

$$\begin{aligned} \frac{dN}{d\phi} =& \frac{N}{2\pi}\left(1 + 2v_1\cos\phi + 2v_2\cos 2\phi + ...\right) , \\ v_n =& \frac{\int d\phi \cos(n\phi)\frac{dN}{d\phi}}{\int d\phi \frac{dN}{d\phi}} = \langle\cos(n\phi)\rangle , \end{aligned} \tag{1.19}$$

where v_1 is called directed flow and v_2 is elliptical flow. The triangular flow v_3 and higher flow received much attention recently. One of the achievements of this dissertation is a derivation of rapidity-odd from CGC which could lead to directed flow of final particles after hydrodynamics evolution.

1.4 Initial Conditions for HICs

Currently there are two models that are widely used to calculate the initial values of the energy momentum tensor at time of thermalization, the Glauber Model [55] and CGC model [57]. The starting point of both models are usually the Woods-Saxon profiles for the nucleon density in nuclei,

$$\kappa_A(\vec{x}) = \frac{\kappa_0}{1 + \exp[(|\vec{x}| - R)/a]}, \tag{1.20}$$

where κ_0 is a constant that should satisfy $\int d^3x \kappa_A(\vec{x}) = A$, with A being the mass number of colliding nuclei, R is the nuclear radius and a is the skin thickness parameter. For gold (^{197}Au), we have, $R = 6.38$ fm and $a = 0.535$ fm; while for lead (^{207}Pb) we use, $R = 6.62$ fm and $a = 0.546$ fm [55]. It is useful to define a thickness function by integrating the density along the longitudinal axis because of the Lorentz contraction,

$$T_A(\mathbf{x}_\perp) = \int_{-\infty}^{\infty} dz \kappa_A(\vec{x}), \tag{1.21}$$

The Glauber model assumes that in HICs, the initial energy density deposited at position $\mathbf{x}_\perp$ is given by the density of binary nucleon-nucleon collisions n_{coll} and the density of nucleons participating in collisions n_{part}. n_{coll} is the product of the number of nucleons at $\mathbf{x}_\perp$ in one nucleus, the number of nucleons at this position in the other nucleus, and the probability that these nucleons hit each other, i.e.

$$n_{coll}(\mathbf{x}_\perp, b) \sim T_A(x + \frac{b}{2}, y) \times T_A(x - \frac{b}{2}, y) \times \sigma_{NN}(\sqrt{s}), \tag{1.22}$$

where $\sigma_{NN}(\sqrt{s})$ is the nucleon-nucleon cross section. Generally, the energy density

profile of two colliding nuclei is assumed to be a linear combination of binary collision and number of participants, $\epsilon(\mathbf{x}_\perp, b) = \alpha n_{coll}(\mathbf{x}_\perp, b) + \beta n_{part}(\mathbf{x}_\perp, b)$.

Monte-Carlo Glauber models [55] are used to provide event-by-event (E-by-E) initial conditions. The difference between MC-Glauber models and the simple Glauber model above is that, instead of using the average density Eq. (1.20), the actual thickness function for one event is calculated by simulating the positions of nucleons inside the nucleus using the Wood-Saxon distribution. Such E-by-E simulations enable us to study fluctuation effects. Nucleon position fluctuations are crucial for obtaining the observed odd flow coefficients.

The CGC [36, 37] as introduced above is an effective theory of QCD dealing with the saturation physics at low Bjorken-x in high energy nuclear collisions. The cross-section of gluon-gluon scattering in QCD is roughly $\sigma \sim \alpha_s(Q^2)\frac{\pi}{Q^2}$ with Q being the momentum of the gluon. The density of gluons in the transverse plane must be proportional to the number of nucleons over the area $A/(\pi R_0^2)$, where R_0 is the nucleus radius. Gluons will interact with each other strongly if the scattering probability,

$$\frac{A}{\pi R_0^2}\sigma = \alpha_s(Q^2)\frac{A}{R_0^2 Q^2} \sim 1\,. \tag{1.23}$$

is of order 1, where $\alpha_s(Q^2)$ is strong interaction constant. Therefore, one finds that there is a "Saturation" scale $Q_s^2 \sim \alpha_s \frac{A}{R_0^2}$ which define the saturation region. If $Q_s \gg 1$ GeV perturbation theory can be applied.

The most widely used initial conditions inspired by CGC are called the KLN model [56], the transverse energy profile at $\tau = \tau_0$ is given by

$$\epsilon(\mathbf{x}_\perp, b) = \text{const} \times \left[\frac{dN_g}{d^2\mathbf{x}_T dY}(\mathbf{x}_T, b)\right]^{4/3} \tag{1.24}$$

where N_g is the number of gluons produced in the collision,

$$\frac{dN_g}{d^2\mathbf{x}_T dY} \sim \int \frac{d^2\mathbf{p}_T}{p_T^2} \int^{p_T} d^2\mathbf{k}_T \; \alpha_s(k_T) \; \phi_+ \left(\frac{(\mathbf{p}_T + \mathbf{k}_T)^2}{4}; \mathbf{x}_T \right) \; \phi_- \left(\frac{(\mathbf{p}_T - \mathbf{k}_T)^2}{4}; \mathbf{x}_T \right) \tag{1.25}$$

where

$$\phi_\pm(k_T^2; \mathbf{x}_T) = \frac{1}{\alpha_s(Q_s^2)} \frac{Q_s^2}{\max(Q_s^2, k_T^2)} \left(\frac{n_{\text{part}}^A(\mathbf{x}_\perp, \pm b)}{T_A(x \pm b/2, y)} \right) (1-x)^4 \tag{1.26}$$

and $Q_s^2(x, \mathbf{x}_\perp)$ is determined by

$$\frac{2\, T_A^2(x \pm b/2, y)\, \text{GeV}^2}{n_{\text{part}}^A(\mathbf{x}_\perp, \pm b)} \left(\frac{\text{fm}^2}{1.53} \right) \left(\frac{0.01}{x} \right)^{0.288} \tag{1.27}$$

with $x = \frac{p_T}{\sqrt{s}}$. There are also other models based on CGC, for example, the IP-Glasma model [58, 59], which also considers the fluctuation on the nucleon level.

In this dissertation, we will give initial conditions that provides definite initial velocities and shear stress profile with respect to transverse coordinates and space-time rapidity $\eta = \frac{1}{2} \ln \frac{t+z}{t-z}$ from a first principle CGC calculation.

1.5 Outline of the Dissertation

In chapter 2 we first give a brief overview of CGC. After formulating the Yang-Mills equations for the classical gluon fields after the collision, we use a recursive solution in powers of the longitudinal proper time τ [60] and carry the calculation of gluon fields up to 4^{th} order in τ. Comparison with a numerical solution is also shown in this chapter. In chapter 3 we calculate the energy momentum tensor of the gluon fields after the collision and check the energy-momentum conservation up to $\mathcal{O}(\tau^4)$. We generalize the McLerran-Venugopalan Model to go beyond the limit

of large homogenous nuclei in chapter 4. We show that the transverse dynamics on non-perturbative lengths can be safely separated from CGC dynamics. The energy momentum tensor after averaging over color configurations is calculated. In chapter 5, the transverse and longitudinal structure of the Poynting vector field is discussed. Besides the well known radial and elliptic flow in transverse direction, we find a rapidity-odd transverse flow that tilts the fireball for non-central collisions. Instead of just calculating average color configurations, we propose a procedure in chapter 6 to calculate the energy momentum tensor of glasma in an event-by-event framework. Chapter 7 is devoted to matching the energy momentum tensor of the glasma to viscous hydrodynamic initial conditions and the effects of rapidity-odd momentum flow are discussed. We summarize this dissertation in Chapter 8 and present an outlook on future work.

1.6 Useful Definitions

Some conventions and useful formulae used in the following are gathered here. 3-vectors are denoted by bold symbols, vector arrows denote 2-vectors in the transverse plane. E.g. $x^\mu = (t, \mathbf{x}) = (t, \vec{x}_\perp, z)$. Light cone coordinates are defined by

$$x^\pm = \frac{1}{\sqrt{2}} \left(x^0 \pm x^3 \right). \tag{1.28}$$

with $d^4x = dx^+ dx^- d^2x_\perp$ and $x^\mu y_\mu = x^+ y^- + x^- y^+ - x^i_\perp y^i_\perp$. Small Latin indices i indicate transverse components of a vector, i.e. $i = 1, 2$. Note that $\partial^\mu = (\partial/\partial t, -\nabla)$ and $\partial^\pm = \partial/\partial x^\mp$.

Proper time τ and space time rapidity for a space-time point x^μ are defined as

$$\tau = \sqrt{t^2 - z^2} = \sqrt{2x^+x^-}, \tag{1.29}$$

$$\eta = \frac{1}{2}\ln\frac{t+z}{t-z} = \frac{1}{2}\ln\frac{x^+}{x^-}. \tag{1.30}$$

It is useful to express cartesian and light cone derivatives in hyperbolic ones through

$$\partial^\pm = \frac{x^\pm}{\tau}\frac{\partial}{\partial\tau} \mp \frac{1}{2x^\mp}\frac{\partial}{\partial\eta}. \tag{1.31}$$

and

$$\frac{\partial}{\partial t} = \cosh\eta\frac{\partial}{\partial\tau} - \frac{1}{\tau}\sinh\eta\frac{\partial}{\partial\eta}\,, \tag{1.32}$$

$$\frac{\partial}{\partial z} = -\sinh\eta\frac{\partial}{\partial\tau} + \frac{1}{\tau}\cosh\eta\frac{\partial}{\partial\eta}\,. \tag{1.33}$$

The momentum rapidity of a particle is defined as,

$$y = \frac{1}{2}\ln\frac{E+p_z}{E-p_z}. \tag{1.34}$$

2. THE COLOR GLASS CONDENSATE

This chapter is devoted to the classical effective field approach of heavy ion collisions called the color glass condensate. At ultra-relativistic energy, nuclei are highly Lorentz contracted along the direction of motion and the gluons inside the nucleus can be viewed as a thin sheet of color fields. The gluonic evolution time scale is much larger than the time scale of collision, so the gluon fields are treated as "*glass*". The wavefunction of the nuclei is dominated by high density, coherent gluons. Large occupation numbers enable us to describe gluons inside the nuclei as semi-classical color fields.

2.1 The Classical Effective Theory

The fundamental ingredient of CGC is a separation of partons based on their longitudinal momenta $k^+ = xP^+$. Here P^+ is the longitudinal momentum of the nucleon and x is the momentum fraction carried by the parton. The soft partons ($x < x_0$, at RHIC $x_0 \sim 10^{-2}$ and at LHC $x_0 \sim 10^{-4}$ [33]) are treated as the quasi-classical chromo field A^μ generated by fast partons whose x is larger than some scale x_0. The physics should only weakly depend on such separation and a renormalization group equation can be written down to govern changes in x_0, for review refer to [34, 35]. The sources and fields are related by the classical Yang-Mills equations,

$$[D_\mu, F^{\mu\nu}] = J^\nu. \tag{2.1}$$

For a nucleus moving along the positive light cone axis x^+, we can write the components of the currents in light cone coordinates as

$$J^+(x) = \delta(x^-)\rho_1(\vec{x}_\perp), \qquad J^i(x) = 0\,. \tag{2.2}$$

with transverse SU(N_c) charge distributions $\rho(\vec{x}_\perp)$ in the nuclei.

The components of the currents for two nuclei moving in light cone coordinates are

$$J_1^+(x) = \delta(x^-)\rho_1(\vec{x}_\perp)\,, \quad J_1^-(x) = 0 \tag{2.3}$$

$$J_2^-(x) = \delta(x^+)\rho_2(\vec{x}_\perp)\,, \quad J_2^+(x) = 0 \tag{2.4}$$

$$J_{1,2}^i(x) = 0. \tag{2.5}$$

This current fulfills the equation of continuity,

$$[D_\mu, J^\mu] = 0. \tag{2.6}$$

if we choose an axial gauge with

$$x^+A^- + x^-A^+ = 0. \tag{2.7}$$

We will keep this choice of gauge throughout this dissertation except where we specifically mention that we work in covariant gauge.

2.2 General Shape of the Field

Kovner, McLerran and Weigert [62] have first discussed the general space-time structure of the gluon field in the collision of two such nuclei colliding on the light

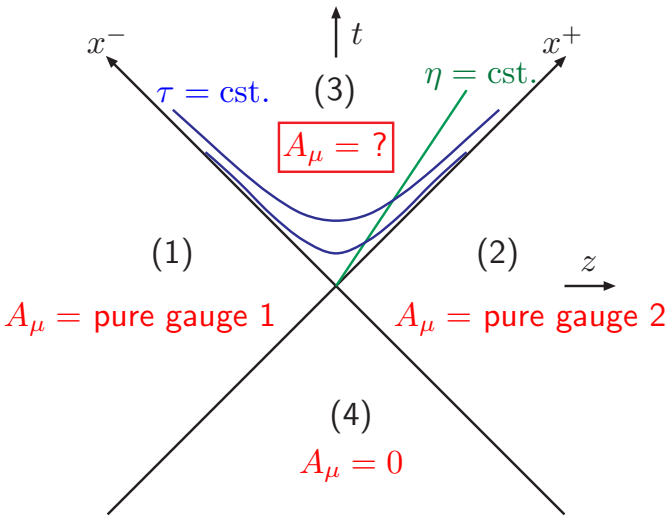

Figure 2.1: Color fields in different region of the lightcone. Figure reprinted from [63] with permission from ELSEVIER.

cone. They have argued that in axial gauge A^μ is a smooth function of x^μ except for the two light cone hypersurfaces with the currents where discontinuities appear. The fields in the backward lightcone (region (4) in Fig. 2.1) vanish, and the fields outside the lightcone (region (2) & (3)) should be pure gauge. It is easy to check that, in the case of one nucleus moving on the light cone, the following field

$$A^{\pm}(x) = 0 \tag{2.8}$$

$$A^i(x) = \Theta(-x^-)\frac{1}{i}U_1(\vec{x}_\perp)\nabla^i U_1^\dagger(\vec{x}_\perp) + \Theta(x^-)\frac{1}{i}U_2(\vec{x}_\perp)\nabla^i U_2^\dagger(\vec{x}_\perp) \tag{2.9}$$

is a solution to the Yang-Mills equations. Where $U_1(\vec{x}_\perp)$ and $U_2(\vec{x}_\perp)$ are different gauge transformations on opposite sides of the sheet at $x^- = 0$. The above solution indicates that the transverse vector potential can be describe by a pure two dimensional gauge transformion.

One thus can write down the following ansatz solution for the fields generated by collision of two nuclei in different regions in the x^+-x^--plane:

$$A^+(x) = \Theta(x^+)\Theta(x^-)x^+A(\tau,\vec{x}_\perp)\,, \tag{2.10}$$

$$A^-(x) = -\,\Theta(x^+)\Theta(x^-)x^-A(\tau,\vec{x}_\perp)\,, \tag{2.11}$$

$$\begin{aligned} A^i(x) =& \Theta(x^-)\Theta(-x^+)A_1^i(\vec{x}_\perp) + \Theta(x^+)\Theta(-x^-)A_2^i(\vec{x}_\perp) \\ &+ \Theta(x^+)\Theta(x^-)A_\perp^i(\tau,\vec{x}_\perp), \end{aligned} \tag{2.12}$$

with $i = 1,2$ is index for transverse coordinates. $A_1^i(\vec{x}_\perp)$ and $A_2^i(\vec{x}_\perp)$ are the gluon fields of the single nuclei before the collision, which are purely transverse in this gauge. $A(\tau,\vec{x}_\perp)$ and $A_\perp^i(\tau,\vec{x}_\perp)$ are smooth functions in the forward light cone and describe the field after the collision. They are the fields we will be interested in. There is no explicit dependence on the space-time rapidity $\eta = 1/2\ln x^+/x^-$ in A and $A_\perp^i$, reflecting the boost-invariance of the system.

In each sector of the light cone the Yang-Mills equations have to be satisfied separately. In the forward light cone they can be written in the convenient form [62]

$$\frac{1}{\tau}\frac{\partial}{\partial\tau}\frac{1}{\tau}\frac{\partial}{\partial\tau}\tau^2 A - \left[D^i,\left[D^i,A\right]\right] = 0\,, \tag{2.13}$$

$$ig\tau\left[A,\frac{\partial}{\partial\tau}A\right] + \frac{1}{\tau}\left[D^i,\frac{\partial}{\partial\tau}A_\perp^i\right] = 0\,, \tag{2.14}$$

$$\frac{1}{\tau}\frac{\partial}{\partial\tau}\tau\frac{\partial}{\partial\tau}A_\perp^i + ig\tau^2\left[A,\left[D^i,A\right]\right] - \left[D^j,F^{ji}\right] = 0\,. \tag{2.15}$$

The field strength tensor in the forward light cone can be expressed in terms of the

gauge potentials A and $A^i_\perp$ in this gauge as

$$F^{+-} = -\frac{1}{\tau}\frac{\partial}{\partial\tau}\tau^2 A, \tag{2.16}$$

$$F^{i\pm} = -x^\pm \left(\frac{1}{\tau}\frac{\partial}{\partial\tau}A^i_\perp \mp [D^i, A]\right), \tag{2.17}$$

$$F^{ij} = \partial^i A^j_\perp - \partial^j A^i_\perp - ig[A^i_\perp, A^j_\perp]. \tag{2.18}$$

Boundary conditions connect different light cone sectors. The ones for the forward light cone read [62]

$$A^i_\perp(\tau = 0, \vec{x}_\perp) = A^i_1(\vec{x}_\perp) + A^i_2(\vec{x}_\perp), \tag{2.19}$$

$$A(\tau = 0, \vec{x}_\perp) = -\frac{ig}{2}\left[A^i_1(\vec{x}_\perp), A^i_2(\vec{x}_\perp)\right]. \tag{2.20}$$

We interpret them as initial conditions for the fields at $\tau = 0$ for the fields in the forward light cone $\tau > 0$.

Eqs. (2.13) through (2.15) together with the conditions (2.19) and (2.20) pose the boundary value problem to be solved. An analytic solution in closed form is not known for the most general case. The weak field or abelian limit was first treated in [62] and will be reproduced below. Several groups have also discussed numerical solutions [64, 65, 66].

A different approach to solve the problem was advocated by Fries et al. in [60, 67]. The basic idea is to focus on analytic solutions for the near-field, i.e. for "small" τ. In that case one can utilize a systematic expansion of the Yang-Mills equation in powers of τ. The rationale is that the approximation of coherent classical fields will not be sufficient anymore after a typical time scale $\sim 1/Q_s$ anyway [68, 69]. At that time decoherence, particle production, particle-field interactions, and eventually thermalization have to be taken into account. We will see that the expansion

technique can actually provide more. One can write down a recursive solution to the field equations that is in principle valid at any arbitrary order in τ.

2.3 τ-Expansion and Recursive Solution

The assumptions justifying the dominance of classical fields in the collision cease to be valid at long times after the collision, $\tau \gg 1/Q_s$. Thus let us define the power series

$$A(\tau, \vec{x}_\perp) = \sum_{n=0}^{\infty} \tau^n A_{(n)}(\vec{x}_\perp), \tag{2.21}$$

$$A^i_\perp(\tau, \vec{x}_\perp) = \sum_{n=0}^{\infty} \tau^n A^i_{\perp(n)}(\vec{x}_\perp). \tag{2.22}$$

We employ an equivalent power series for the field strength, covariant derivatives and the energy-momentum tensor. Eqs. (2.13) – (2.15) permit a set of singular solutions, but only the solutions regular at $\tau = 0$ are physical solutions for the boundary value problem.

Let us discuss this point for the abelianized version of the equations in more detail. In the case of weak fields the non-linear terms in the YM equations can be neglected, leading to a greatly simplified, abelian version of the boundary value problem for which an analytic solution in closed form can be given [61, 62]. After dropping the non-linear terms and applying a Fourier transformation of the transverse coordinate, $\partial^i \to -ik^i_\perp$, equations (2.13) and (2.15) take the shape of Bessel equations

$$\frac{1}{z}\frac{d^2}{dz^2} zA + \frac{1}{z^2}\frac{d}{dz} zA + \frac{1}{z} zA - \frac{1}{z^3} zA = 0 \tag{2.23}$$

$$z^2 \frac{d^2}{dz^2} A^i_\perp + z\frac{d}{dz} A^i_\perp + z^2 A^i_\perp = 0 \tag{2.24}$$

where $z = k_\perp \tau$ and with a physical polarization $\nabla^i A^i_\perp = 0$ chosen for the transverse

vector [62]. There are two independent sets of solutions, Bessel functions of the first kind $A \sim J_1(z)/z$, $A^i_\perp \sim J_0(z)$ which are regular at $\tau = 0$, and Neumann functions $A \sim N_1(z)/z$, $A^i_\perp \sim N_0(z)$ which lead to $A \sim z^{-2}$ and a singularity $A^i_\perp \sim \ln \tau$ for $\tau \to 0$. The solution with Neumann functions is not compatible with Eq. (2.14) which imposes $\partial/\partial\tau A^i_\perp = 0$. The singular solution therefore has to be excluded. It is easy to see that the non-abelian field equations do not change this argument.

Let us now return to the solution of the general non-abelian problem. The power series turns the set of 3 differential equations (2.13), (2.14), (2.15) in $x_\perp$ and τ into an infinite system of differential equations in $x_\perp$. As first shown by Fries, Kapusta and Li [60], we can solve this system recursively. The boundary conditions (2.19), (2.20) provide the starting point of the recursion

$$A^i_{\perp(0)} = A^i_1 + A^i_2 \,, \tag{2.25}$$

$$A_{(0)} = -\frac{ig}{2}\left[A^i_1, A^i_2\right] \,. \tag{2.26}$$

Next one can prove that all odd-power contributions vanish, $A_{(2k+1)} = 0$, $A^i_{\perp(2k+1)} = 0$. Finally, one finds the recursion relations for even n, $n > 1$,

$$A_{(n)} = \frac{1}{n(n+2)} \sum_{k+l+m=n-2} \left[D^i_{(k)}, \left[D^i_{(l)}, A_{(m)}\right]\right] , \tag{2.27}$$

$$\begin{aligned} A^i_{\perp(n)} = \frac{1}{n^2} \Bigg(& \sum_{k+l=n-2} \left[D^j_{(k)}, F^{ji}_{(l)}\right] \\ & + ig \sum_{k+l+m=n-4} \left[A_{(k)}, [D^i_{(l)}, A_{(m)}]\right] \Bigg) \,. \end{aligned} \tag{2.28}$$

One can easily check that these expressions solve (2.13) - (2.15).

One can use the abelianized case for a cross check. After dropping non-linear terms and after applying a Fourier transformation to the transverse coordinates the

recursive solutions can be easily resummed to give

$$A^{\mathrm{LO}}_{(n)} = \frac{2}{n!!^2(n+2)}(-k_\perp^2)^{n/2}A^{\mathrm{ab}}_{(0)}\,, \quad (n>1) \tag{2.29}$$

$$A^{\mathrm{LO}i}_{\perp(n)} = \frac{1}{n!!^2}(-k_\perp^2)^{n/2}A^{\mathrm{LO}i}_{\perp(0)} \tag{2.30}$$

where the double factorial is $n!! = n(n-2)(n-4)\cdots$ and the index LO signals the abelian case. These terms are just the coefficients of the Bessel functions already discussed above,

$$A^{\mathrm{LO}}(\tau,\mathrm{k}_\perp) = \frac{2A^{\mathrm{LO}}_{(0)}(\mathrm{k}_\perp)}{k_\perp\tau}J_1\left(k_\perp\tau\right) \tag{2.31}$$

$$A^{\mathrm{LO}i}_{\perp}(\tau,\mathrm{k}_\perp) = A^{\mathrm{LO}i}_{\perp(0)}(\mathrm{k}_\perp)J_0\left(k_\perp\tau\right)\,. \tag{2.32}$$

Hence we have shown that the small-τ expansion works for all τ in the abelian case.

2.4 The Near Field

A resummation similar to the abelian case seems elusive for the general solution. Nevertheless one can analyze the few lowest order terms which are equivalent to describing the "near field" close to the light cone. We do this in terms of the more physical field strength tensor. The near field up to order τ^3 order has been worked out by Fries et al [61]. We observe that only the longitudinal components of the electric and magnetic chromofield have non-vanishing values at $\tau = 0$:

$$E^3_{(0)} = F^{+-}_{(0)} = ig\left[A^i_1, A^i_2\right]\,, \tag{2.33}$$

$$B^3_{(0)} = F^{21}_{(0)} = ig\epsilon^{ij}\left[A^i_1, A^j_2\right]\,. \tag{2.34}$$

We denote these initial values briefly with $E_0 \equiv E^3_{(0)}$ and $B_0 \equiv B^3_{(0)}$ to emphasize their importance as the "seed" values for $\tau \to 0$. The transverse fields vanish at $\tau = 0$: $F^{i\pm}_{(0)} = 0$.

The dominance of longitudinal fields at early times has been rediscovered a few years back [70] and has since then been discussed as the reason for a variety of physical effects. The color flux tubes associated with these fields could lead to particle production via the Schwinger mechanism [71], imply non-trivial topological configurations [72, 73], and induce long-range rapidity correlations. It also is a posteriori justification for the color capacitor picture. Interestingly the longitudinal magnetic field can be of the same size as the longitudinal electric field.

The next order $\mathcal{O}(\tau^1)$ brings no further contribution to the longitudinal fields, $F^{+-}_{(1)} = 0 = F^{21}_{(1)}$, but it is the leading order for the transverse fields

$$F^{i\pm}_{(1)} = -\frac{e^{\pm\eta}}{2\sqrt{2}} \left([D^j_{(0)}, F^{ji}_{(0)}] \pm [D^i_{(0)}, F^{+-}_{(0)}] \right) . \tag{2.35}$$

Hence the transverse electric and magnetic chromofields grow linearly from their zero value at $\tau = 0$. We can express them in terms of the initial longitudinal fields as

$$E^i_{(1)} = -\frac{1}{2} \left(\sinh\eta [D^i, E_0] + \cosh\eta \, \epsilon^{ij} [D^j, B_0] \right) \tag{2.36}$$

$$B^i_{(1)} = \frac{1}{2} \left(\cosh\eta \, \epsilon^{ij} [D^j, E_0] - \sinh\eta [D^i, B_0] \right) . \tag{2.37}$$

Note that we suppress the index (0) on transverse covariant derivatives in the following and write $D^i \equiv \partial^i - igA^i_{\perp(0)}$, unless noted otherwise.

Fries et al also computed the next-to-leading correction in τ to all components [61]. The first correction to the initial value of the longitudinal fields appears at

order $\mathcal{O}(\tau^2)$ and is in our short notation

$$E^3_{(2)} = \frac{1}{4}[D^i, [D^i, E_0]]\,, \tag{2.38}$$

$$B^3_{(2)} = \frac{1}{4}[D^i, [D^i, B_0]]\,. \tag{2.39}$$

There is no correction to the transverse fields at this order, $F^{i\pm}_{(2)} = 0$. Generally, the longitudinal fields have only contributions for even powers of τ, the transverse fields pick up contributions exclusively for odd powers of τ. From generalizing to all orders in τ we can also conclude that the longitudinal electric and magnetic fields are independent of η while the transverse fields are a superposition of terms depending on $\cosh\eta$ and $\sinh\eta$.

Going beyond previous work by Fries et al [60], we calculated the order τ^3 results [74]. The order $\mathcal{O}(\tau^3)$ for the transverse fields are

$$F^{i\pm}_{(3)} = -\frac{e^{\pm\eta}}{4\sqrt{2}}\left([D^j, F^{ji}_{(2)}] \pm [D^i, F^{+-}_{(2)}]\right) + \frac{ig}{8}\left(\epsilon^{ij}[B_0, F^{j\pm}_{(1)}] \pm [E_0, F^{i\pm}_{(1)}]\right) \mp \frac{ig}{8}\frac{e^{\pm\eta}}{2\sqrt{2}}\epsilon^{ij}[D^j, [E_0, B_0]] \tag{2.40}$$

whereas $E^3_{(3)} = 0 = B^3_{(3)}$. In terms of the initial fields the third order fields are

$$\begin{aligned} E^i_{(3)} =& -\frac{1}{16}\left(\cosh\eta\,\epsilon^{ij}[D^j, [D^k, [D^k, B_0]]] + \sinh\eta\,[D^i, [D^k, [D^k, E_0]]]\right) \\ &- \frac{ig}{16}\epsilon^{ij}\sinh\eta\left([B_0, [D^j, E_0]] + [E_0, [D^j, B_0]]\right) \\ &- \frac{ig}{16}\cosh\eta\left([E_0, D^i, E_0] - [B_0, [D^i, B_0]]\right) \\ &- \frac{ig}{16}\sinh\eta\epsilon^{ij}[D^j, [E_0, B_0]]\,, \end{aligned} \tag{2.41}$$

$$
\begin{aligned}
B^i_{(3)} = &-\frac{1}{16}\left(\sinh\eta[D^i,[D^k,[D^k,B_0]]]-\cosh\eta\epsilon^{ij}[D^j,[D^k,[D^k,E_0]]]\right)\\
&-\frac{ig}{16}\cosh\eta\left([B_0,[D^i,E_0]]+[E_0,[D^i,B_0]]\right)\\
&-\frac{ig}{16}\sinh\eta\epsilon^{ij}\left([B_0,[D^j,B_0]]-[E_0,[D^j,E_0]]\right)\\
&-\frac{ig}{16}\cosh\eta[D^i,[E_0,B_0]]\,.
\end{aligned}
$$

The longitudinal field survives at order $\mathcal{O}(\tau^4)$ are

$$
\begin{aligned}
E^3_{(4)} =&\frac{1}{64}[D^i,[D^i,[D^j,[D^j,E_0]]]]+\frac{1}{16}ig\epsilon^{ij}[[D^i,E_0],[D^j,B_0]]\,,\\
B^3_{(4)} =&\frac{1}{64}[D^i,[D^i,[D^j,[D^j,B_0]]]]-\frac{1}{64}ig\epsilon^{ij}[[D^i,E_0],[D^j,E_0]]\\
&+\frac{3}{64}ig\epsilon^{ij}[[D^i,B_0],[D^j,B_0]]\,.
\end{aligned}
$$

Our explicit expressions provide truncated expressions which approximate the full solutions to an accuracy

$$E^3 = E^3_{\text{trunc}} + \mathcal{O}(\tau^6)\,, \tag{2.42}$$

$$E^i = E^i_{\text{trunc}} + \mathcal{O}(\tau^5) \tag{2.43}$$

for the electric field. The same scheme holds for the magnetic field $\vec{B}$. Explicit expressions for even higher powers of τ could in principle be derived from the recursion relations (2.27) and (2.28).

2.5 Comparison to Numerical Results

We just make a few remarks on how numerical solutions of the Yang-Mills equation quantitatively confirm important aspects of the series expansion in τ. We com-

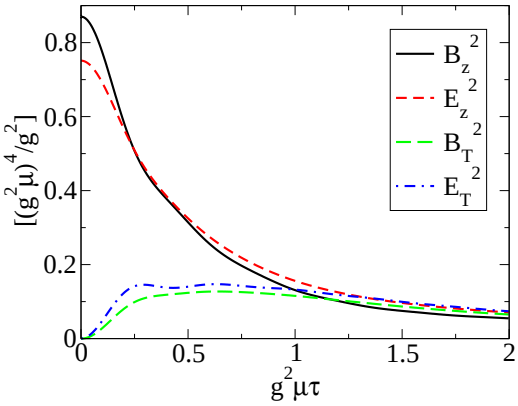

Figure 2.2: Squares of components of the color field as function of τ in a numerical calculation by Lappi. Figure reprinted from [63] with permission from ELSEVIER.

pare our results to numerical solutions of the classical Yang-Mills equations obtained by Lappi [63]. Fig. 2.2 shows the squares of longitudinal and transverse electric and magnetic fields. Immediately after the collision, there are only longitudinal fields which decrease as τ increases. The transverse fields build up linearly for small τ. The growth is cut off when τ^3 terms become important and the increase will stop. We note that the key features of these fields are provided by the small-τ expansion if terms up to τ^4 are considered. Initially, at $\tau = 0$, the value of longitudinal fields should be given by the τ^0 order series expansion E_0 and B_0. The τ^2 terms account for the rapid decrease of longitudinal fields as τ increases for small τ. The τ^4 order terms should be positive and will approximately determine the inflection point for the longitudinal fields in Fig. 2.2. The cut off in the slope of transverse fields is almost a straight line for very small τ, which confirms that the behavior is dominated by the first order in τ. The τ^3 terms will increase. In short, the longitudinal fields can be written as a $a\tau^4 - b\tau^2 + c$ function and transverse fields can be fitted

by $a'\tau - b'\tau^3$ function for $0 < g^2\mu\tau < 0.5$ [1] with $a, a', b, b', c > 0$. In the following sections we will determine these coefficients in more detail.

[1]Note that the color charge density μ defined in this work (see Chapter 4 for definition) corresponds to μ^2 in Lappi's notation.

3. THE ENERGY MOMENTUM TENSOR OF THE FIELD

From the field strength tensor we can easily calculate the energy momentum tensor of the field

$$T^{\mu\nu} = F^{\mu\lambda}F^{\nu}_{\lambda} + \frac{1}{4}g^{\mu\nu}F^{\kappa\lambda}F_{\kappa\lambda}\,. \tag{3.1}$$

For brevity we employ a notation where $\mathrm{SU}(N_c)$ indices are summed over implicitly unless said otherwise. Thus $AB = A^aB^a = 2\,\mathrm{Tr}(AB)$, $a = 1, \ldots, N_c^2 - 1$, are equivalent notations for a singlet formed from the contraction of two $\mathrm{SU}(N_c)$ objects A and B. We discuss the first few orders in τ of the components of the tensor.

3.1 Components of the Energy Momentum Tensor up to Order τ^2

3.1.1 Order τ^0

It is straightforward to see that only the diagonal elements of $T^{\mu\nu}$ have finite values at $\tau = 0$. We define ε_0 to be the initial value for the energy density

$$\varepsilon_0 = T^{00}_{(0)} = \frac{1}{2}\left(E_0^2 + B_0^2\right) = -\frac{g^2}{2}\left(\delta^{ij}\delta^{kl} + \epsilon^{ij}\epsilon^{kl}\right)\left([A_1^i, A_2^j][A_1^k, A_2^l]\right) \tag{3.2}$$

The other diagonal elements of the energy momentum tensor are

$$T^{11}_{(0)} = T^{22}_{(0)} = \varepsilon_0 \tag{3.3}$$

$$T^{33}_{(0)} = -\varepsilon_0 \tag{3.4}$$

Hence the structure of the energy momentum tensor for $\tau \to 0$ is the same as that for a longitudinal field in classical electrodynamics. There is a maximum "pressure" anisotropy between the transverse and longitudinal directions. Despite being far from equilibrium we take the liberty to use the notations of longitudinal pressure

$p_L = T^{33}$ and transverse pressure $p_T = T^{11} = T^{22}$. We find the transverse pressure to be very large, $p_T = \varepsilon_0$, compared to an equilibrated system (an ideal relativistic gas with the same energy density would have a transverse pressure $p_T = \epsilon_0/3$) while the longitudinal pressure $p_L = -p_T = -\varepsilon_0$ is equally large and negative.

The sign of the longitudinal pressure is not surprising. It means that there is a deceleration of the nuclei, as if a plates of the "color capacitor" are being pulled together by the longitudinal fields. This is the mechanism that removes kinetic energy from the nuclei and deposits it as field strength between them. However keep in mind that in our setup we do not calculate the field and the motion of the nuclei selfconsistently. We assume that they move along the light cone undisturbed. The BRAHMS experiment has reported that the initial nuclei (represented by the baryon number in the system) lose about 70 to 75% of their kinetic energy in collisions of gold nuclei at RHIC [75]. This means the nuclei or their fragments stay ultrarelativistic throughout the collision and it is a viable approximation to keep their motion fixed on the light cone.

The qualitative behavior of the system is then clear from the simple form of $T^{\mu\nu}$ for $\tau \to 0$. While the negative longitudinal pressure leads to the *deceleration* of the colliding nuclei, the transverse pressure forces the system to *expand* in transverse direction. This transverse expansion can happen immediately, without any need for equilibration or decoherence. In fact the transverse pressure is 3 times larger than naively assumed. If the fields decohere and thermalize, the longitudinal pressure p_L has to change sign. In fact this change of sign has to happen fast enough since otherwise the deceleration work $dW = p_L dV$ done on the nuclear debris would become too large and lead to a yo-yo effect.

3.1.2 Order τ^1

At the next order $\mathcal{O}(\tau^1)$ the components T^{0i} and T^{3i} are the only ones to pick up contributions. They describe the flow of energy and longitudinal momentum into the transverse direction. Note that T^{0i} is the transverse component of the Poynting vector $\vec{S} = \vec{E} \times \vec{B}$. Therefore the expected transverse expansion sets in linearly in τ. We have

$$\begin{aligned} T^{0i}_{(1)} =& \epsilon^{ij} \left(B_0 E^j_{(1)} - E_0 B^j_{(1)} \right) \qquad (3.5) \\ =& \frac{1}{2} \cosh \eta \, \alpha^i + \frac{1}{2} \sinh \eta \, \beta^i \,, \\ T^{3i}_{(1)} =& - E_0 E^i_{(1)} - B_0 B^i_{(1)} \qquad (3.6) \\ =& \frac{1}{2} \sinh \eta \, \alpha^i + \frac{1}{2} \cosh \eta \, \beta^i \,. \end{aligned}$$

Recall that we agreed to omit the index (0) on covariant derivatives: $D^i = \partial^i - igA^i_{\perp(0)}$.

We notice that we have two contributions to the flow. The first term is the flow driven by the gradient of the transverse pressure as we would expect from a hydrodynamic picture

$$\alpha^i = -\nabla^i \varepsilon_0 \,. \qquad (3.7)$$

The second term involves the 2-vector

$$\beta^i = \epsilon^{ij} \left([D^j, B_0] E_0 - [D^j, E_0] B_0 \right) \,. \qquad (3.8)$$

It is anomalous in the sense that it is not driven by the transverse pressure and enters the energy momentum tensor as a rapidity-odd flow. It can, among other things, lead to directed flow and has been first presented in [76] and is discussed in detail in

[77]. We will explore its meaning in Chapter 5.

3.1.3 Order τ^2

At the order $\mathcal{O}(\tau^2)$ the diagonal elements of $T^{\mu\nu}$ receive their first corrections and all the previously vanishing components acquire their leading contribution. On the other hand the transverse flow of energy and longitudinal momentum is not affected,

$$T^{0i}_{(2)} = 0 = T^{3i}_{(2)} \,. \tag{3.9}$$

The expressions for the energy density, the longitudinal flow of energy and the flow of longitudinal momentum are

$$\begin{aligned}
T^{00}_{(2)} =& E_0 E^3_{(2)} + B_0 B^3_{(2)} + \frac{1}{2} E^i_{(1)} E^i_{(1)} + \frac{1}{2} B^i_{(1)} B^i_{(1)} \\
=& -\frac{1}{4}(\nabla^i \alpha^i + \delta) - \frac{1}{8} \sinh 2\eta \, \nabla^i \beta^i + \frac{1}{8} \cosh 2\eta \delta \,, \qquad (3.10) \\
T^{03}_{(2)} =& \epsilon^{ij} E^i_{(1)} B^j_{(1)} \qquad (3.11) \\
=& -\frac{1}{8} \cosh 2\eta \, \nabla^i \beta^i + \frac{1}{8} \sinh 2\eta \, \delta \,, \\
T^{33}_{(2)} =& -E_0 E^3_{(2)} - B_0 B^3_{(2)} + \frac{1}{2} E^i_{(1)} E^i_{(1)} + \frac{1}{2} B^i_{(1)} B^i_{(1)} \\
=& \frac{1}{4}(\nabla^i \alpha^i + \delta) - \frac{1}{8} \sinh 2\eta \, \nabla^i \beta^i + \frac{1}{8} \cosh 2\eta \, \delta \,. \qquad (3.12)
\end{aligned}$$

The only new combination of fields appearing is related to longitudinal flow and reads

$$\delta = [D^i, E_0][D^i, E_0] + [D^i, B_0][D^i, B_0] \,. \tag{3.13}$$

Clearly δ is a measure for longitudinal flow of energy which does not mix with transverse flow at this order in τ. On the other hand we see that the flow β^i couples transverse and longitudinal degrees of freedom. We will discuss energy and

momentum conservation in more detail below.

The results for the remaining new contributions to this order are

$$\begin{aligned} T^{ii}_{(2)} =& \frac{(-1)^i}{2}\left(E^1_{(1)}E^1_{(1)} + B^1_{(1)}B^1_{(1)}\right. \\ & \left. -E^2_{(1)}E^2_{(1)} - B^2_{(1)}B^2_{(1)}\right) + E_0E^3_{(2)} + B_0B^3_{(2)} \\ =& -\frac{1}{4}(-\triangle\epsilon_0 + \delta + \omega_i)\,, \end{aligned} \tag{3.14}$$

$$T^{12}_{(2)} = -E^1_{(1)}E^2_{(1)} - B^1_{(1)}B^2_{(1)} = \gamma\,. \tag{3.15}$$

$\triangle$ here is the 2-dimensional Laplace operator. There is no implicit summation over the double index $i = 1, 2$ in the first equation. The new quantities are

$$\begin{aligned} \omega_i =& \frac{(-1)^i}{2}\left([D^1, E_0]^2 - [D^2, E_0]^2\right. \\ & \left. + [D^1, B_0]^2 - [D^2, B_0]^2\right)\,, \end{aligned} \tag{3.16}$$

$$\gamma = [D^1, E_0][D^2, E_0] + [D^1, B_0][D^2, B_0]\,. \tag{3.17}$$

Note that ω_i does not transform like a 2-vector. In the last equations one has to be careful not to confuse upper vector indices 2 with squares.

3.2 Order τ^3 and τ^4.

At order τ^3 the only contributions are the first corrections for the transverse flow components T^{0i} and T^{3i}. They are

$$\begin{aligned} T^{0i}_{(3)} =& \epsilon^{ij}\left(B_0 E^j_{(3)} + B^3_{(2)} E^j_{(1)} - E_0 B^j_{(3)} - E^3_{(2)} B^j_{(1)}\right) \\ =& \frac{1}{16}\left(\cosh\eta\,\xi^i + \sinh\eta\,\zeta^i\right)\,, \end{aligned} \tag{3.18}$$

$$\begin{aligned} T^{3i}_{(3)} =& -E_0 E^i_{(3)} - E^3_{(2)} E^i_{(1)} - B_0 B^i_{(3)} - B^3_{(2)} B^i_{(1)} \\ =& \frac{1}{16}\left(\sinh\eta\,\xi^i + \cosh\eta\,\zeta^i\right)\,. \end{aligned} \tag{3.19}$$

The transverse flow vectors ξ^i and ζ^i defined in Eq. (3.19) are given in terms of E_0 and B_0 by

$$\begin{aligned} \xi^i =& \left[D^i, E_0[D^l,[D^l,E_0]] + B_0[D^l,[D^l,B_0]]\right] + [D^i,E_0][D^l,[D^l,E_0]] \\ &+ [D^i,B_0][D^l,[D^l,B_0]] - ig\epsilon^{ij}B_0[E_0,[D^j,E_0]]\,, \end{aligned} \tag{3.20}$$

$$\begin{aligned} \zeta^i =& \epsilon^{ij}\left(\left[D^j,E_0[D^l,[D^l,B_0]] - B_0[D^l,[D^l,E_0]]\right] - 3[D^j,E_0][D^l,[D^l,B_0]]\right. \\ &\left. + 3[D^j,B_0][D^l,[D^l,E_0]]\right) - 3igE_0[B_0,[D^i,B_0]]\,. \end{aligned} \tag{3.21}$$

At order τ^4 corrections to the energy density, longitudinal flow of momentum and longitudinal flow of energy are

$$T^{00}_{(4)} = \rho + \kappa\frac{1}{32}\cosh 2\eta + \sigma\frac{1}{32}\sinh 2\eta\,, \tag{3.22}$$

$$T^{33}_{(4)} = -\rho + \kappa\frac{1}{32}\cosh 2\eta + \sigma\frac{1}{32}\sinh 2\eta \tag{3.23}$$

$$T^{03}_{(4)} = \sigma\frac{1}{32}\cosh 2\eta + \kappa\frac{1}{32}\sinh 2\eta \tag{3.24}$$

Where

$$
\begin{aligned}
\rho =& B_0 B_{(4)} + E_0 E_{(4)} + \frac{1}{2}(B_{(2)} B_{(2)} + E_{(2)} E_{(2)}) \\
\kappa =& [D^i, B_0][D^i, [D^k, [D^k, B_0]]] + [D^i, E_0][D^i, [D^k, [D^k, E_0]] \\
& + ig\epsilon^{ij}[D^i, B_0]([B_0, [D^j, B_0]] - [E_0, [D^j, E_0]]) \\
& + ig\epsilon^{ij}[D^i, E_0]([B_0, [D^j, E_0]] + [E_0, [D^j, B_0]] + [D^j, [E_0, B_0]]]) \\
\sigma =& \epsilon^{ij}[D^i, E_0][D^j, [D^k, [D^k, B_0]]] \\
& - \epsilon^{ij}[D^i, B_0][D^j, [D^k, [D^k, E_0]]] \\
& + ig[D^i, B_0]([B_0, [D^i, E_0]] \\
& + [E_0, [D^i, B_0]] + [D^i, [E_0, B_0]]) \\
& + ig[D^i, E_0]([E_0, [D^i, E_0]] - [B_0, [D^i, B_0]])
\end{aligned}
$$

This completes the list of contributions we have calculated. The truncated series for the energy momentum tensor presented here is accurate up to corrections of order $\mathcal{O}(\tau^5)$ for the T^{0i} and T^{3i} components and of order $\mathcal{O}(\tau^6)$ for all other components.

3.3 Checking Energy and Momentum Conservation

The solutions of the Yang-Mills equations automatically satisfy energy and momentum conservation, i.e. $\partial_\mu T^{\mu\nu} = 0 +$ corrections of higher order in τ. This can be checked explicitly order by order. $\partial_\mu T^{\mu 0}$ and $\partial_\mu T^{\mu 3}$ receive contributions only for odd powers of τ, whereas $\partial_\mu T^{\mu i}$ exclusively consists of even powers.

Transverse momentum conservation, $\nu = 1, 2$, is obvious at order τ^0. From the

corresponding equation

$$\begin{aligned}\partial_\mu T^{\mu i}\Big|_{\tau^0} =& \left(\cosh\eta - \sinh\eta\frac{\partial}{\partial\eta}\right) T^{0i}_{(1)} \\ &- \left(\sinh\eta - \cosh\eta\frac{\partial}{\partial\eta}\right) T^{3i}_{(1)} + \nabla^i T^{ii}_{(0)} \\ =&\alpha^i + \nabla^i\varepsilon_0\,.\end{aligned} \tag{3.25}$$

all terms containing the anomalous flow β^i drop out and the remaining expression obviously vanishes using the known result for the hydrodynamic flow α^i. Note that the index i is not summed in the term containing T^{ii}.

At order τ^1 we have,

$$\begin{aligned}\partial_\mu T^{\mu 0}\Big|_{\tau^1} =& (\cosh\eta\frac{\partial}{\partial\tau} - \frac{1}{\tau}\sinh\eta\frac{\partial}{\partial\eta})T^{00}_{(2)} \\ &+ (-\sinh\eta\frac{\partial}{\partial\tau} + \frac{1}{\tau}\cosh\eta\frac{\partial}{\partial\eta})T^{30}_{(2)} + \nabla^i T^{i0}_{(1)} \\ =& -\frac{1}{2}\cosh\eta(\nabla^i\alpha^i + \delta) \\ &+ \frac{1}{2}\cosh\eta(-\sinh 2\eta\nabla^i\beta^i + \cosh 2\eta\delta) \\ &- \frac{1}{2}\sinh\eta(-\cosh 2\eta\nabla^i\beta^i + \sinh 2\eta\delta) \\ &+ \frac{1}{2}\cosh\eta\nabla^i\alpha^i + \frac{1}{2}\sinh\eta\nabla^i\beta^i \\ =&0\,.\end{aligned} \tag{3.26}$$

The proof for $\nu = 3$ is completely analogous.

At order τ^2 we have a very similar picture

$$\begin{aligned}\partial_\mu T^{\mu i}\Big|_{\tau^2} =& \left(3\cosh\eta - \sinh\eta\frac{\partial}{\partial\eta}\right) T^{0i}_{(3)} \\ &- \left(3\sinh\eta - \cosh\eta\frac{\partial}{\partial\eta}\right) T^{3i}_{(3)} \\ &+ \nabla^i T^{ii}_{(2)} + \nabla^j T^{ji}_{(2)} \\ =&\xi^i - \nabla^i\left(-\triangle\epsilon_0 + \delta + \omega_i\right) + \nabla^j\gamma\,.\end{aligned} \tag{3.27}$$

with the anomalous flow contributions ζ^i canceling. Again, the index $i = 1, 2$ is not summed upon multiple appearance and in addition we define j to be the transverse index with $j \neq i$. Momentum conservation holds if the equation

$$\xi^i = \nabla^i\left(-\triangle\epsilon_0 + \delta + \omega_i\right) - \nabla^j\gamma\,. \tag{3.28}$$

is true. We can check it explicitly:

$$\begin{aligned}&\nabla^x\left(-\triangle\epsilon_0 + \delta + \omega_x\right) - \nabla^y\gamma \\ =& -\nabla^x\big(((E_0[D^l,[D^l,E_0]] + B_0[D^l,[D^l,B_0]]) \\ &+ ([D^l,E_0][D^l,E_0] + [D^l,B_0][D^l,B_0]) \\ &- ([D^l,E_0][D^l,E_0] + [D^l,B_0][D^l,B_0])\big) \\ &+ \frac{1}{2}\big([D^x,[D^x,E_0]^2] + [D^x,[D^x,B_0]^2] \\ &- [D^y,[D^y,E_0]^2] - [D^y,[D^y,B_0]^2]\big) \\ &+ [D^y,[D^x,E_0][D^y,E_0] + [D^x,B_0][D^y,B_0]] \\ =&\big[D^x,E_0[D^l,[D^l,E_0]] + B_0[D^l,[D^l,B_0]]\big] \\ &+ [D^x,E_0][D^l,[D^l,E_0]] + [D^1,B_0][D^l,[D^l,B_0]] = \xi^x\end{aligned} \tag{3.29}$$

Overall we have now established that our truncated expression for the energy momentum tensor satisfies

$$\partial_\mu T^{\mu 0} = 0 + \mathcal{O}(\tau^3)\,, \tag{3.30}$$

$$\partial_\mu T^{\mu i} = 0 + \mathcal{O}(\tau^4)\,, \tag{3.31}$$

$$\partial_\mu T^{\mu 3} = 0 + \mathcal{O}(\tau^3)\,. \tag{3.32}$$

We are confident that this is a solid basis for further analysis.

So far we have held the charge distributions ρ_k in the two nuclei fixed and have expressed the fields and the energy momentum tensor after the collision in terms of the initial fields E_0 and B_0. E_0 and B_0 are in turn determined by the gauge potentials A_k^i in the two nuclei before the collision using our choice of axial gauge. In a given nuclear collision the color charge densities are not known. In fact when integrating over transverse space the total color charge should be zero, and if we look at the expectation value (or long time average) of ρ_k^i in nucleus k at any fixed point in the transverse plane it should vanish as well, $\langle \rho_k^i \rangle = 0$. However fluctuations can result in non-vanishing color charge at a given point in time and space. The internal dynamics of the fluctuations are much slower than the time scale of the high energy collision such that we can treat the ρ_k^i as frozen but random with average fluctuation strength $\langle \rho_k^i \rho_l^i \rangle = \mu \delta_{kl}$ where $\mu > 0$ is an average squared color charge density. This opens the way to two possible implementations. We could analyze random samples of charge densities with Monte-Carlo methods. This will lead to an event-by-event determination of the energy momentum tensor. Such MC techniques have recently been explored in [59]. We will investigate this option in Chapter 6. Here we calculate expectation values for observables which will allow us to analytically study important aspects.

In this and the following chapter we will ensemble-average classical gluon fields over all possible charge distributions with the conditions above and calculate expectation values. For an observable O measured after the collision of two nuclei this would be

$$\langle O \rangle_{\rho_1,\rho_2} = \int d[\rho_1] d[\rho_2] O(\rho_1, \rho_2) w(\rho_1) w(\rho_2) \tag{4.1}$$

where the w are appropriate weights. In the McLerran-Venugopalan model the weight functions are chosen to have the simplest Gaussian shape

$$w(\rho_k) = e^{-\int d^2x_\perp \rho_k^2(\vec{x}_\perp)/2g^2\mu_k}\,, \tag{4.2}$$

where the fluctuation strength is set by average densities $g^2\mu_k$.

The averaging corresponds to a random walk in the space of SU(N_c) valued functions. In the following we will calculate these expectation values for the energy momentum tensor using a slightly generalized McLerran Venugopalan model.

4.1 The McLerran Venugopalan Model with Transverse Dynamics (MVTD)

We start with a brief review of the MV model. We implement the averaging over color sources in a given nucleus by fixing the expectation value

$$\langle \rho_{\underline{a}}(x^\mp, \vec{x}_\perp)\rho_{\underline{b}}(y^\mp, \vec{y}_\perp)\rangle = \frac{g^2}{(N_c^2-1)}\delta_{\underline{ab}}\lambda(x^\mp, \vec{x}_\perp)\delta(x^\mp - y^\mp)\delta^2(\vec{x}_\perp - \vec{y}_\perp), \tag{4.3}$$

for a nucleus moving along the $+$ or $-$ light cone respectively, together with the condition that expectation values of any odd number of ρ-fields vanish. We drop the index k labeling a particular nucleus here for ease of notation. We have explicitly written out the coupling constant g that was contained in ρ as defined in Eqs. (2.1) and (2.3). λ and μ are then number densities summed over color degrees of freedom. Note that the normalization of μ differs by a factor N_c^2-1 from many other definitions in the literature [63]. We allow a dependence of the expectation value on both the longitudinal coordinate $x^\mp$ and the transverse coordinate $\vec{x}_\perp$.

The longitudinal smearing is necessary to compute expectation values correctly as first realized in [78]. A nucleus has to be given a small, but finite, thickness across

the light cone which we will do by introducing

$$\lambda(x^{\mp}, \vec{x}_\perp) = \mu(\vec{x}_\perp) h(x^{\pm}) \tag{4.4}$$

where h is a non-negative function with finite width ϵ around $x^{\pm} = 0$ such that

$$\int dx^- \lambda(x^-, \vec{x}_\perp) = \mu(\vec{x}_\perp)\,. \tag{4.5}$$

We do not need to specify it further (but we could imagine e.g. a Gaussian of width ϵ).

We have introduced the dependence of the area charge density μ on $\vec{x}_\perp$ as a generalization of the assumptions of the proper McLerran-Venugopalan model, where the nuclei are infinitely large in the transverse direction and on average invariant under rotations and translations. Real nuclei break these symmetries, and it is a worthwhile goal to investigate the stability of the MV results under small deviations from these symmetries. Our motivation here is that no transverse dynamics can be generated in the strict MV model.

We will allow the following relaxation of the MV conditions: in each domain of size $\sim 1/m$ in the transverse plane μ is *almost* constant, more precisely we want that

$$|\mu(\vec{x}_\perp)| \gg m^{-1} \left|\nabla^i \mu(\vec{x}_\perp)\right| \gg m^{-2} \left|\nabla^i \nabla^j \mu(\vec{x}_\perp)\right| \gg \dots\,. \tag{4.6}$$

The purpose here is that inside domains of size $1/m$ the well-defined physics of the color glass is applicable, while on length scales larger than $1/m$ unrelated infrared behavior is allowed to occur. Fig. 4.1 shows that the first inequality in Eq. (4.6) is true for more than 90% of matter in a nucleus if reasonable values of the infrared

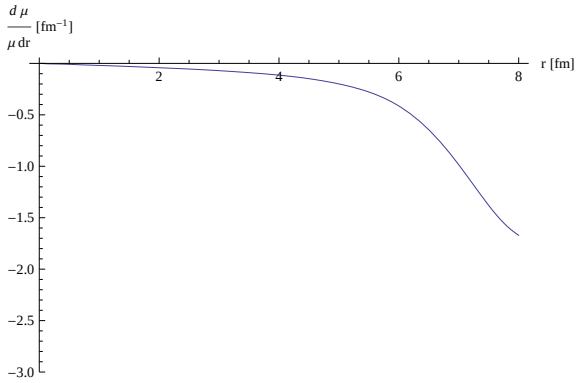

Figure 4.1: The ratio of gradients of charge density over charge density for a realistic gold nucleus with Woods-Saxon profile. Eq. (4.6) is true for more than 90% of matter in a nucleus if a realistic infrared cutoff 1 fm^{-1} $\sim$ 200 MeV is chosen.

scale are chosen. Thus we imagine a hierarchy

$$1/Q_s \ll 1/m \ll R_A \tag{4.7}$$

and m hence is an infrared scale which separates color glass physics from long-range QCD.

We have two main goals in this expanded McLerran-Venugopalan (MVTD) model: (i) Results must be well behaved under these small deviations from translational and rotational invariance, otherwise the original MV model would not be infrared safe. In practice this means that observables should be only weakly dependent on the infrared scale. We will explicitly check this condition below. (ii) The results will provide a long-range dynamics, expanded in gradients of μ, which is compatible with color glass physics at small distances. This will allow us to safely apply the MV model locally to realistic nuclei as long as the location is sufficiently far away from

the boundary of the nucleus where the density μ starts to fall off quickly. We also have a chance to address the consequences of inhomogeneities in the transverse plane as long as their typical length scale is larger than the typical color glass length scale. It is this feature that will allow us to calculate flow in color glass.

4.2 The Gluon Distribution

The most important expectation value is the two-point gluon function, or gluon distribution $\langle A^i_{\underline{a}}(\vec{x}_\perp) A^i_{\underline{a}}(\vec{y}_\perp)\rangle$ in light cone gauge. The Yang-Mills equations (2.1) for a single nucleus on the +-light cone are most easily solved in a covariant gauge where $A^\mu_{\rm cov} = \delta^{\mu +}\alpha$. The equations then reduce to

$$\Delta\alpha(x^-, \vec{x}_\perp) = -\rho_{\rm cov}(x^-, \vec{x}_\perp) \tag{4.8}$$

where the Laplace operator Δ acts on the transverse directions. The explicit solution is

$$\alpha(x^-, \vec{x}_\perp) = \int dz_\perp^2 G(\vec{x}_\perp - z_\perp)\rho_{\rm cov}(x^-, \vec{z}_\perp) \tag{4.9}$$

with a Green's function $G(x_\perp) = -\ln(x_\perp^2/\Lambda^2)/(4\pi)$ where Λ is an arbitrary length scale. However, we will be better served by introducing a physically motivated regularization through a gluon mass m which can be inserted into the Fourier transformation of the Green's function $\tilde{G}(k) = 1/k^2 \to 1/(k^2 + m^2)$ [79]. [1] This leads to the representation

$$G(x_\perp) = \frac{1}{2\pi} K_0(m x_\perp) \tag{4.10}$$

using Bessel functions K_0. This Green's function reproduces the previous expression in the limit $m \to 0$ with $\Lambda = 2e^{-\gamma_E}/m$, where γ_E is Euler's constant. The two-gluon

[1] Note that the gluon mass could be an unrelated infrared scale but for simplicity we choose the IR cutoff in the gradient expansion of μ to be identical.

correlation function in covariant gauge as the average of two gluon fields can then be easily derived from (4.3) as

$$\langle \alpha_{\underline{a}}(x^-, \vec{x}_\perp)\alpha_{\underline{b}}(y^-, \vec{y}_\perp)\rangle = \frac{g^2}{N_c^2 - 1}\delta_{\underline{ab}}\delta(x^- - y^-)\gamma(x^-, \vec{x}_\perp, \vec{y}_\perp) \tag{4.11}$$

where we have introduced the Green's function

$$\gamma(x^-, \vec{x}_\perp, \vec{y}_\perp) = \int d^2\vec{z}_\perp G(\vec{x}_\perp - \vec{z}_\perp)G(\vec{y}_\perp - \vec{z}_\perp)\lambda(x^-, \vec{z}_\perp)\,. \tag{4.12}$$

We will show below that γ depends strongly on the IR regularization scale m. It diverges like $1/m^2$ in the limits $|\vec{x} - \vec{y}| \to 0$.

The gluon field A^i in light cone gauge can be derived from the covariant expression with the help of the Wilson line

$$U(x^-, x_\perp) = \mathcal{P}\exp\left[-ig\int_{-\infty}^{x^-}\alpha(z^-, \vec{x}_\perp)dz^-\right]. \tag{4.13}$$

Here $\mathcal{P}$ denotes path ordering of the fields α from right to left. One can show that the correct gauge transformation to arrive at the light cone potential is [78].

$$A^i(x^-, \vec{x}_\perp) = \frac{i}{g}U(x^-, \vec{x}_\perp)\partial^i U^\dagger(x^-, \vec{x}_\perp) \tag{4.14}$$

This enables us to calculate the expectation value of a pair of gluons in the MV model in the light cone gauge which is related to the gluon distribution

$$\langle F^{+i}_{\underline{a}}(x^-, \vec{x}_\perp)F^{+j}_{\underline{b}}(y^-, \vec{y}_\perp)\rangle = \left\langle \left(\mathcal{U}^\dagger_{\underline{ac}}\partial^i\alpha_{\underline{c}}\right)(x^-, \vec{x}_\perp)\left(\mathcal{U}^\dagger_{\underline{bd}}\partial^j\alpha_{\underline{d}}\right)(y^-, \vec{y}_\perp)\right\rangle . \tag{4.15}$$

In this equation we have used gauge transformations $F = UF_{\rm cov}U^\dagger$ to covariant

gauge and then expressed the Wilson lines U by their counterparts in the adjoint representation, $\mathcal{U}$, by virtue of the relation

$$U t_{\underline{a}} U^\dagger = \mathcal{U}_{\underline{ab}} t_{\underline{b}} \,. \tag{4.16}$$

Let us take a small detour here to discuss expectation values of adjoint, parallel Wilson lines in the MV model [78]. A systematic study was recently carried out by Fukushima and Hidaka [80]. For a single line we get

$$\langle \mathcal{U}_{\underline{ab}}(x^-, \vec{x}_\perp) \rangle = \delta_{\underline{ab}} \exp\left[-\frac{g^4 N_c}{2(N_c^2-1)} \times \int_{-\infty}^{x^-} \gamma(z^-, \vec{x}_\perp, \vec{x}_\perp) dz^- \right]. \tag{4.17}$$

This expectation value is suppressed since $\gamma(z^-, \vec{x}_\perp, \vec{y}_\perp)$ tends to diverge in the limit $m \to 0$.

For a double line we have

$$\left\langle \mathcal{U}_{\underline{ab}}(x^-, \vec{x}_\perp) \mathcal{U}_{\underline{cd}}(x^-, \vec{y}_\perp) \right\rangle = \delta_{\underline{ad}} \delta_{\underline{bc}} d(x^-, \vec{x}_\perp, \vec{y}_\perp) \tag{4.18}$$

where

$$\Gamma(z^-, \vec{x}_\perp, \vec{y}_\perp) = 2\gamma(z^-, \vec{x}_\perp, \vec{y}_\perp) - \gamma(z^-, \vec{x}_\perp, \vec{x}_\perp) - \gamma(z^-, \vec{y}_\perp, \vec{y}_\perp) \,. \tag{4.19}$$

is a subtracted version of γ, and

$$d(x^-, \vec{x}_\perp, \vec{y}_\perp) = \exp\left[\frac{g^4 N_c}{2(N_c^2-1)} \int_{-\infty}^{x^-} dz^- \Gamma(z^-, \vec{x}_\perp, \vec{y}_\perp) \right] \tag{4.20}$$

is the exponentiation of the integral of Γ along the light cone. In the original MV model the subtraction in Γ removes the $1/m^2$ singularity in γ for small m and renders

the exponential d finite. In particular, $\Gamma(x^-, \vec{x}_\perp, \vec{y}_\perp)$ vanishes in the ultraviolet limit $\vec{y}_\perp \to \vec{x}_\perp$. We will show below that this crucial cancellation is still valid for our generalization. Here we have also dropped contributions from non-color singlet pairs [80].

We return to the discussion of the correlation function of fields. One can prove that the only possible contraction of fields on the right hand side of (4.15) comes from a factorization into correlators $\sim \langle \mathcal{U}^\dagger \mathcal{U}^\dagger \rangle \langle \partial^i \alpha \partial^j \alpha \rangle$. The latter factor can be derived from (4.11)

$$\langle \partial^i \alpha_{\underline{a}}(x^-, \vec{x}_\perp) \partial^j \alpha_{\underline{b}}(y^-, \vec{y}_\perp) \rangle = \frac{g^2}{N_c^2 - 1} \delta_{\underline{ab}} \delta(x^- - y^-) \nabla_x^i \nabla_y^j \gamma(x^-, \vec{x}_\perp, \vec{y}_\perp) \,. \tag{4.21}$$

This leads to the result

$$\begin{aligned} \langle F_{\underline{a}}^{+i}(x^-, \vec{x}_\perp) F_{\underline{b}}^{+j}(y^-, \vec{y}_\perp) \rangle = \frac{g^2}{N_c^2 - 1} \delta_{\underline{ab}} \delta(x^- - y^-) \\ \times \left[\nabla_x^i \nabla_y^j \gamma(x^-, \vec{x}_\perp, \vec{y}_\perp) \right] d(x^-, \vec{x}_\perp, \vec{y}_\perp) \end{aligned} \tag{4.22}$$

for the expectation value of fields in light cone gauge. The correlation function of two gauge potentials in light cone gauge follows from an integration with retarded boundary conditions

$$A^i(x^-, \vec{x}_\perp) = - \int_{-\infty}^{x^-} dz^- F^{+i}(z^-, \vec{x}_\perp) \,. \tag{4.23}$$

One integral is easily taken to give

$$\langle A^i_{\underline{a}}(x^-,\vec{x}_\perp)A^j_{\underline{b}}(y^-,\vec{y}_\perp)\rangle = g^2\delta_{\underline{ab}}\frac{2\nabla^i_x\nabla^j_y\gamma(\vec{x}_\perp,\vec{y}_\perp)}{g^4N_c\Gamma(\vec{x}_\perp,\vec{y}_\perp)} \times\int_{-\infty}^{\min\{x^-,y^-\}}dx'^-\frac{\partial}{\partial x^-}\exp\left[\frac{g^4N_c}{2(N_c^2-1)}\Gamma(\vec{x}_\perp,\vec{y}_\perp)\int_{-\infty}^{x'^-}dz^-h(z^-)\right]. \quad (4.24)$$

Note that we have taken a factor $h(x^-)$ from both γ and Γ and we have rewritten one factor of $h(x^-)$ as a derivative $\partial/\partial x^-$ of the exponential. We formally define γ [and Γ] $(\vec{x}_\perp,\vec{y}_\perp)$ as the integral of γ [and Γ] $(x^-,\vec{x}_\perp,\vec{y}_\perp)$ over x^- from $-\infty$ to $+\infty$, respectively.

We can then take the second integral. We will only be interested in $\min\{x^-,y^-\} > 0$ and upon taking the limit of vanishing width ϵ of h we have

$$\langle A^i_{\underline{a}}(\vec{x}_\perp)A^j_{\underline{b}}(\vec{y}_\perp)\rangle = 2g^2\delta_{\underline{ab}}\frac{\nabla^i_x\nabla^j_y\gamma(\vec{x}_\perp,\vec{y}_\perp)}{g^4N_c\Gamma(\vec{x}_\perp,\vec{y}_\perp)} \times\left(\exp\left[\frac{g^2N_c}{2(N_c^2-1)}\Gamma(\vec{x}_\perp,\vec{y}_\perp)\right]-1\right). \quad (4.25)$$

This result holds for both the McLerran-Venugopalan model [78] and our generalization. For further evaluation we have to understand the correlations functions γ and Γ. We will calculate them next. Before we proceed let us briefly write down the gluon distribution function in the ultraviolet limit $\vec{y}_\perp \to \vec{x}_\perp$. In that limit $\Gamma \to 0$, and we can expand the exponential function around 0 using only the two leading terms to arrive at the simple expression

$$\langle A^i_{\underline{a}}(\vec{x}_\perp)A^j_{\underline{b}}(\vec{x}_\perp)\rangle = \delta_{\underline{ab}}\frac{g^2}{N_c^2-1}\nabla^i_x\nabla^j_y\gamma(\vec{x}_\perp,\vec{y}_\perp)\Big|_{\vec{y}_\perp\to\vec{x}_\perp}. \quad (4.26)$$

4.3 Gluon Fields in the Generalized MV Model

The cancellation of the singularity in γ through the subtraction in Eq. (4.19) is a classic result of the proper McLerran-Venugopalan model. We will now show that this benign result holds for the inhomogeneous charge densities λ that we have permitted. This will also prove that the original assumptions of the MV model regarding homogenous charge distributions are well defined, since stable under small perturbations. Let us introduce center and relative coordinates for two points $\vec{x}_\perp$ and $\vec{y}_\perp$ in the transverse plane via $\vec{R} = (\vec{x}_\perp + \vec{y}_\perp)/2$ and $\vec{r} = \vec{y}_\perp - \vec{x}_\perp$.

We first recall the argument in the original McLerran-Venugopalan model. For constant $\mu(\vec{x}_\perp) = \mu_0$ we need to calculate the correlation function

$$\begin{aligned}\gamma_0(r) \equiv \gamma_0(\vec{x}_\perp, \vec{y}_\perp) &= \mu_0 \int d^2 z_\perp G(\vec{x}_\perp - \vec{z}_\perp) G(\vec{y}_\perp - \vec{z}_\perp) \\ &= \mu_0 \int \frac{d^2 k_\perp}{(2\pi)^2} e^{i\vec{k}_\perp \vec{r}} \frac{1}{(k_\perp^2 + m^2)^2} = \lambda_0 \frac{r}{4\pi m} K_1(mr) \quad (4.27)\end{aligned}$$

which only depends on the relative distance r due to isotropy and translational invariance . Due to the factorization of $h(x^-)$ all results also hold for the correlation functions not integrated over x^-. As mentioned before γ_0 exhibits a quadratic dependence on the infrared cutoff m for small r. In particular, we have $\gamma_0(0) = \lambda_0/(4\pi m^2)$. Hence the subtracted 2-point function (4.19) in this case, in the ultraviolet limit $r \to 0$ becomes

$$\Gamma_0(r) = 2\gamma_0(r) - 2\gamma_0(0) = \mu_0 \frac{r^2}{8\pi} \left(\ln \frac{r^2 m^2}{4} + 2\gamma_E - 1 \right) + \mathcal{O}(m^2 r^4)\,. \quad (4.28)$$

This is equivalent to the result in [78] using a finite gluon mass regularization. The power singularity $1/m^2$ is replaced by a weak logarithmic dependence on m for small

r.

Let us now check that the same cancellation takes place if λ is weakly varying on length scales $1/m$ as permitted above. We are only interested in typical values of $r = |\vec{y}_\perp - \vec{x}_\perp| \lesssim Q_s^{-1}$ since the inverse distance should be larger than the infrared regulator, $r^{-1} \gg m$. In fact the computation of the energy momentum tensor only requires the limit $mr \ll 1$ (which we have called the ultraviolet limit). Next we recall that the Green functions $G(z_\perp) \sim K_0(mz_\perp)$ fall off on a scale $\sim 1/m \gg r$. Under these conditions, we can restrict ourselves to the first few terms of a Taylor expansion of μ around $\vec{R}$ in the calculation of γ:

$$\mu(\vec{z}_\perp) = \mu(\vec{R}) + (\vec{z}_\perp - \vec{R})^i \nabla^i \mu(\vec{R}) + \dots \tag{4.29}$$

which leads to the expression

$$\gamma(\vec{R}, \vec{r}) \equiv \gamma(\vec{x}_\perp, \vec{y}_\perp) = \gamma_0(\vec{R}, r) + \frac{1}{2} \nabla^i \nabla^j \mu(\vec{R}) \gamma^{ij}(\vec{r}) + \dots . \tag{4.30}$$

Here we have $\gamma_0(\vec{R}, r) = \mu(\vec{R}) r K_1(mr)/(4\pi m)$ analogous to (4.27), representing the constant term. The linear term vanishes due to

$$\int d^2\vec{z}_\perp G(\vec{z}_\perp + \vec{r}/2) G(\vec{z}_\perp - \vec{r}/2) z_\perp^i = 0 \,, \tag{4.31}$$

and the second order term is

$$\gamma^{ij} = \int d^2\vec{z}_\perp G(\vec{z}_\perp) G(\vec{r} - \vec{z}_\perp) z_\perp^i z_\perp^j = \delta^{ij} \frac{r^2}{24\pi m^2} K_2(mr) + \frac{r^i r^j}{r^2} \frac{13 r^3}{96\pi m} K_1(mr) \tag{4.32}$$

These correlations functions can be conveniently computed in Fourier space, similar to the technique in Eq. (4.27).

The subtraction of $\gamma(0)$ removes the leading quadratically divergent term in m as in the original McLerran-Venugopalan model. In the relevant limit $rm \to 0$ we have

$$\Gamma(\vec{R},\vec{r}) = \lambda(\vec{R})\frac{r^2}{8\pi}\left(\ln \hat{m}^2 r^2 - 2\right) + \mathcal{O}(\lambda m^2 r^4) + \nabla^i\nabla^j\ \lambda(\vec{R})\left[-\delta^{ij} + \frac{r^i r^j}{r^2}\frac{13}{2}\right]\frac{r^2}{48\pi m^2} + \mathcal{O}([\nabla^2\lambda]m^0 r^4) + \mathcal{O}(\nabla^4\lambda)\,. \quad (4.33)$$

where $\hat{m} = \kappa m$ and $\kappa = \exp(\gamma_E + 1/2)/2 \approx 1.47$. Indeed, the dependence on the cutoff m is at most logarithmic for the small variations of λ that are permitted. Note that we will never keep gradients of μ larger than order 2 since higher orders will be hard to control phenomenologically.

Besides the subtracted correlation function Γ we need to check the double derivative $\nabla_x^i\nabla_y^j\gamma(\vec{x},\vec{y})$ in the gluon distribution (4.26). Up to second order gradients we obtain

$$\nabla_x^i\nabla_y^j\gamma(\vec{x},\vec{y}) = \mu(\vec{R})\frac{1}{4\pi}\left[\delta^{ij}K_0(mr) - \frac{r^i r^j}{r^2}mrK_1(mr)\right] + \left[-\nabla^i\nabla^j\mu(\vec{R})\frac{7}{2} + \triangle\mu(\vec{R})\delta^{ij}\right]\frac{r}{48\pi m}K_1(mr) + \mathcal{O}(\nabla^3\mu)\,. \quad (4.34)$$

We take the limit $mr \to 0$ and keep only terms isotropic in $\vec{r}$ by setting $r^i r^j/r^2 \to \delta^{ij}/2$, as no dependence on the direction of $\vec{r}$ should remain in this limit. The leading terms of the correlation function with two derivatives read

$$\nabla_x^i\nabla_y^j\gamma(\vec{R},r)\Big|_{r\to 0} = -\mu(\vec{R})\frac{1}{8\pi}\delta^{ij}\ln(\hat{m}^2 r^2) + \left[-\nabla^i\nabla^j\mu(\vec{R})\frac{7}{2} + \triangle\mu(\vec{R})\delta^{ij}\right]\frac{1}{48\pi m^2}\,, \quad (4.35)$$

where $\hat{m} = e\bar{m} \approx 1.47m$

Eqs. (4.33), (4.34) together with (4.25) or (4.26) determine the gluon distribution in the generalized McLerran-Venugopalan model. For the case of constant μ we recover the standard expression for the gluon distribution [78, 63]

$$\langle A^i_{\underline{a}} A^i_{\underline{a}} \rangle = \frac{4(N_c^2-1)}{g^2 N_c r^2} \left(1 - (\hat{m}^2 r^2)^{\frac{g^4 N_c}{16\pi(N_c^2-1)}\mu r^2} \right) . \tag{4.36}$$

Recall that our definition of μ has an additional factor $N_c^2 - 1$ compared to [78, 63]. The generalized result in the ultraviolet limit is

$$\langle A^i_{\underline{a}}(\vec{x}_\perp) A^j_{\underline{b}}(\vec{x}_\perp) \rangle = \delta_{\underline{ab}} \frac{g^2 \mu(\vec{x})}{8\pi(N_c^2-1)} \left[\delta^{ij} \ln \frac{Q^2}{\hat{m}^2} + \frac{\nabla^k \nabla^l \mu(\vec{x})}{m^2 \mu(\vec{x})} \left(\frac{1}{6}\delta^{kl}\delta^{ij} - \frac{7}{12}\delta^{ik}\delta^{jl} \right) \right] . \tag{4.37}$$

up to second order in gradients. Here we have regularized the limit $r \to 0$ by an ultraviolet cutoff $Q \sim 1/r$ in the logarithm.

4.4 Higher Twist Gluon Correlation Functions

For the components of the energy momentum tensor beyond the leading term in the τ expansion we will need expectation values of expressions of the gluon field beyond the gluon distribution function. We will compute those correlation functions in this subsection. With more fields or more derivatives they are akin to "higher twist" gluon distributions, and we will see that there is indeed a power counting hierarchy.

With one additional transverse derivative in the 2-gluon correlation function we

have

$$\langle \partial^k A^i_{\underline{a}}(x^-,\vec{x}_\perp) A^j_{\underline{b}}(y^-,\vec{y}_\perp)\rangle = \int_{-\infty}^{x^-} dx'^- \int_{-\infty}^{y^-} dy'^- \left(\left\langle (D^k F^{+i})_{\underline{a}}(x'^-,\vec{x}_\perp) F^{+j}_{\underline{b}}(y'^-,\vec{y}_\perp) \right\rangle \right.$$
$$\left. + ig \left\langle \left[A^k, F^{+i}\right]_{\underline{a}}(x'^-,\vec{x}_\perp) F^{+j}_{\underline{b}}(y'^-,\vec{y}_\perp) \right\rangle \right) . \quad (4.38)$$

Using the same change to covariant gauge as in Sec. 4.2 the first and second expectation value can be transformed into

$$\left\langle \mathcal{U}^\dagger_{\underline{a}\underline{a}'}(x'^-,\vec{x}_\perp) \mathcal{U}^\dagger_{\underline{b}\underline{b}'}(y'^-,\vec{y}_\perp) \partial^k \partial^i \alpha_{\underline{a}'}(x'^-,\vec{x}_\perp) \partial^j \alpha_{\underline{b}'}(y'^-,\vec{y}_\perp) \right\rangle$$
$$= \delta_{\underline{a}\underline{b}} \frac{g^2}{N_c^2-1} \delta(x'^- - y'^-) \left[-\nabla^i_x \nabla^k_x \nabla^j_y \gamma(x'^-,\vec{x}_\perp,\vec{y}_\perp) \right] d(x'^-,\vec{x}_\perp,\vec{y}_\perp) , \quad (4.39)$$

$$i f_{\underline{c}\underline{d}\underline{a}} \int_{-\infty}^{x^-} dx''^- \left\langle F^{+k}_{\underline{c}}(x''^-,\vec{x}_\perp) F^{+i}_{\underline{d}}(x'^-,\vec{x}_\perp) F^{+j}_{\underline{b}}(y^-,\vec{y}_\perp) \right\rangle$$
$$= i f_{\underline{c}\underline{d}\underline{a}} \int_{-\infty}^{x^-} dx''^- \left\langle \mathcal{U}^\dagger_{\underline{c}\underline{c}'}(x''^-,\vec{x}_\perp) \mathcal{U}^\dagger_{\underline{d}\underline{d}'}(x'^-,\vec{x}_\perp) \mathcal{U}^\dagger_{\underline{b}\underline{b}'}(y'^-,\vec{y}_\perp) \right.$$
$$\left. \times \partial^k \alpha_{\underline{c}'}(x''^-,\vec{x}_\perp) \partial^i \alpha_{\underline{d}'}(x'^-,\vec{x}_\perp) \partial^j \alpha_{\underline{b}'}(y'^-,\vec{y}_\perp) \right\rangle = 0 , \quad (4.40)$$

respectively. The second term vanishes since an even number of adjoint Wilson lines and fields α have to be contracted with each other (combinations $\langle U\alpha\rangle \sim 0$ are suppressed) [80]. For the first term we recall that in covariant gauge $D^k_{\rm cov} F^{+i}_{\rm cov} = \partial^k \partial^i \alpha$. The two integrals over x'^- and y^- can be dealt with exactly as in the case of the gluon distribution. The result for arbitrary longitudinal positions $x^- > 0$ (after taking the thickness ϵ of light cone sources to zero) in the relevant UV limit is

$$\langle \partial^k A^i_{\underline{a}}(\vec{x}_\perp) A^j_{\underline{b}}(\vec{x}_\perp)\rangle = -\frac{g^2}{N_c^2-1} \delta_{\underline{a}\underline{b}} \nabla^i_x \nabla^k_x \nabla^j_y \gamma(\vec{x}_\perp,\vec{y}_\perp)\Big|_{\vec{y}_\perp \to \vec{x}_\perp} . \quad (4.41)$$

Similarly we can treat two more expectation values with 2 derivatives each. We obtain

$$\langle \partial^k A^i_{\underline{a}}(\vec{x}_\perp)\partial^l A^j_{\underline{b}}(\vec{x}_\perp)\rangle = \frac{g^2\delta_{\underline{ab}}}{(N_c^2-1)}\Bigg[\nabla^i_x\nabla^k_x\nabla^j_y\nabla^l_y\gamma(\vec{x}_\perp,\vec{y}_\perp) + \frac{g^2N_c}{2(N_c^2-1)}\nabla^i_x\nabla^j_y\gamma(\vec{x}_\perp,\vec{y}_\perp)\nabla^k_x\nabla^l_y\gamma(\vec{x}_\perp,\vec{y}_\perp)\Bigg]_{\vec{y}_\perp\to\vec{x}_\perp}. \quad (4.42)$$

The expectation value can be written as a sum of four terms $\sim DFDF$, $\sim FFDF$, $\sim DFFF$, $FFFF$ as in (4.39). The second and third vanish for the same reasons the second term in (4.39) dissappears. The other two terms can be shown to correspond to the two contributions in the equation above. In the same spirit we have

$$\langle \partial^k\partial^l A^i_{\underline{a}}(\vec{x}_\perp)A^j_{\underline{b}}(\vec{x}_\perp)\rangle = \frac{g^2\delta_{\underline{ab}}}{(N_c^2-1)}\Bigg[\nabla^i_x\nabla^k_x\nabla^l_x\nabla^j_y\gamma(\vec{x}_\perp,\vec{y}_\perp) - \frac{g^2N_c}{2(N_c^2-1)} \times \nabla^i_x\nabla^j_y\gamma(\vec{x}_\perp,\vec{y}_\perp)\nabla^k_x\nabla^l_x\gamma(\vec{x}_\perp,\vec{x}_\perp)\Bigg]_{\vec{y}_\perp\to\vec{x}_\perp}. \quad (4.43)$$

The higher derivatives of the correlation function γ are straightforward to calculate. We have

$$\nabla^i_x\nabla^k_x\nabla^j_y\gamma(\vec{x}_\perp,\vec{y}_\perp) = \frac{\mu(\vec{R})}{4\pi}\left[\left(\delta^{ij}\frac{r^k}{r}+\delta^{ik}\frac{r^j}{r}+\delta^{jk}\frac{r^i}{r}\right)mK_1(mr)\frac{r^ir^jr^k}{2r^3}m^2rK_2(mr)\right] + \frac{\nabla^l\mu(\vec{R})}{8\pi}\left(\delta^{jl}\frac{r^ir^k}{r^2}-\delta^{il}\frac{r^jr^k}{r^2}-\delta^{kl}\frac{r^ir^j}{r^2}\right)mrK_1(mr) - \frac{\nabla^l\mu(\vec{R})}{8\pi}\left(\delta^{jl}\delta^{ik}-\delta^{il}\delta^{jk}-\delta^{kl}\delta^{ij}\right)K_0(mr) \quad (4.44)$$

where we have kept the two leading orders, $\sim 1/r$ and $\sim m$, in our power counting in mr. One can check that the contribution of the leading term to observables (e.g. to β^i) vanishes due to the odd number of powers in r^i. Hence the relevant term in

the UV limit is

$$\nabla_x^i \nabla_{x,y}^k \nabla_y^j \gamma(\vec{x}_\perp, \vec{y}_\perp)\big|_{\vec{y}_\perp \to \vec{x}_\perp} = \frac{\nabla^l \mu(\vec{R})}{16\pi} \ln \frac{Q^2}{\hat{m}^2} \left(\mp \delta^{jl}\delta^{ik} \pm \delta^{il}\delta^{jk} + \delta^{kl}\delta^{ij} \right) . \tag{4.45}$$

The lower signs are valid if the derivative ∇^k acts on $y_\perp$ instead of $x_\perp$. As discussed above we have dropped a term $\mathcal{O}(g^2\mu Q)$ that does not contribute to observables. One can check from the lower signs in (4.45) that $\langle A^i_{\underline{a}} \partial^k A^j_{\underline{b}}(\vec{x}_\perp)\rangle$ has the same form modulo a permutation $\{i, \underline{a}\} \leftrightarrow \{j, \underline{b}\}$ consistent with the symmetry of the expression.

Caution is needed when we are calculating four derivatives on γ. The leading behavior of $\nabla_x^i \nabla_y^j \nabla_x^k \nabla_{x,y}^l \gamma(\vec{x}_\perp, \vec{y}_\perp)\big|_{\vec{y}_\perp \to \vec{x}_\perp}$ is similar to $\triangle \ln r$ which vanishes every where excerpt $r \to 0$. A proper integration will give us the leading term, together with the next leading term, we have (again regularizing $1/r$ by Q),

$$\begin{aligned} \nabla_x^i \nabla_y^j \nabla_x^k \nabla_{x,y}^l \gamma(\vec{x}_\perp, \vec{y}_\perp)\big|_{\vec{y}_\perp \to \vec{x}_\perp} = & \mp \frac{\mu(\vec{R})}{4\pi} Q^2 \frac{1}{8} \left(\delta^{ij}\delta^{kl} + \delta^{ik}\delta^{jl} + \delta^{jk}\delta^{il} \right) \\ & + \frac{\nabla^m \nabla^n \mu(\vec{R})}{32\pi} \ln \frac{Q^2}{\hat{m}^2} (\delta^{ij}\delta^{km}\delta^{ln} - \delta^{ik}\delta^{jm}\delta^{ln} \\ & \mp \delta^{il}\delta^{jm}\delta^{kn} + \delta^{jk}\delta^{im}\delta^{ln} \pm \delta^{jl}\delta^{im}\delta^{kn} \mp \delta^{kl}\delta^{im}\delta^{jn}) . \end{aligned} \tag{4.46}$$

The leading term only depends on the charge density at the transverse position while the next leading term depends on 2^{nd} gradients on charge density, which essentially contribute to energy momentum tensor at the same order of $\nabla^i \alpha^i$ and $\nabla^i \beta^i$. Thus we have all the ingredients to calculate expectation values of components of the energy momentum tensor up to 2^{nd} order in time which we will do in the next chapter.

5. ENERGY MOMENTUM TENSOR AND FLOW OF GLASMA

We now return to the case of two colliding nuclei and calculate expectation values for the energy momentum tensor. We will further break down the expressions for the components of the energy momentum tensor in the small time expansion in terms of the initial longitudinal fields such that they can be written in terms of the fields A_1^i and A_2^i in the individual nuclei. It is then straightforward to apply the results of the last section to obtain the proper expectation values that can be observed in nuclear collisions. [1]

5.1 Energy Density and Flow

The expectation value of the initial energy density ϵ_0 from Eq. (3.2) can be written as [63],

$$\varepsilon_0 \equiv \langle \varepsilon_0 \rangle = \frac{g^2}{2} f_{\underline{abe}} f_{\underline{cde}} \left(\delta^{ij}\delta^{kl} + \epsilon^{ij}\epsilon^{kl} \right) \langle A^i_{1,\underline{a}} A^k_{1,\underline{c}} \rangle_{\rho_1} \langle A^j_{2,\underline{b}} A^l_{2,\underline{d}} \rangle_{\rho_2} \,. \tag{5.1}$$

Note that in this chapter we calculate only averages of components of the energy momentum tensor and will henceforth suppress the symbol $\langle \ldots \rangle$ in the notation for simplicity.

Applying (4.37) for each nucleus the initial energy density is

$$\varepsilon_0(\vec{x}_\perp) = T^{00}_{(0)}(\vec{x}_\perp) = \frac{g^6 N_c}{32\pi^2(N_c^2-1)} \mu_1(\vec{x}_\perp)\mu_2(\vec{x}_\perp) \ln^2 \frac{Q^2}{\hat{m}^2} \equiv c_0 \mu_1(\vec{x}_\perp)\mu_2(\vec{x}_\perp) \,. \tag{5.2}$$

μ_1 and μ_2 are the expectation values of the densities of charges, as discussed in the

[1] Part of the contents in this chapter is reprinted from *Global flow of glasma in high energy nuclear collisions* by G. Chen and R. J. Fries, 2013, Phys. Lett. B, 723, 417-420. Copyright [2013] by Elsevier.

last section, in nuclei 1 and 2, respectively. We have dropped terms $\sim \nabla\nabla\mu/m^2$ subleading for the energy density.

We have defined the coefficient c_0 as,

$$c_0 = \frac{g^6 N_c}{32\pi^2(N_c^2-1)} \ln^2 \frac{Q^2}{\hat{m}^2} \,. \tag{5.3}$$

Eq. (5.2) is consistent with the expression derived by Lappi in [63] up to a factor of $(N_c^2-1)^2$ coming from different definition of charge density μ.

The expectation value of flow in transverse direction at order $\mathcal{O}(\tau)$ is given by

$$\alpha^i = -c_0 \nabla^i \left(\mu_1 \mu_2\right) \,, \tag{5.4}$$

for rapidity-even contribution. We assume here that we can choose Q^2 and $\hat{m}$ universally and that they do not depend on $\vec{x}_\perp$. If $Q = Q_s$ that would not be true. The rapidity odd flow vector needs to be evaluated with the same technique as the energy density. Separation of contributions from both nuclei leads to

$$\begin{aligned}\beta^i = g^2 f_{\underline{abe}} f_{\underline{cde}} \epsilon^{ij} \left(\epsilon^{mn}\delta^{kl} - \epsilon^{kl}\delta^{mn}\right) \big[&\langle(\partial^i A^m_{1,\underline{a}}) A^k_{1,\underline{c}}\rangle \langle A^n_{2,\underline{b}} A^l_{2,\underline{d}}\rangle \\ &+ \langle(A^m_{1,\underline{a}}) A^k_{1,\underline{c}}\rangle \langle(\partial A^n_{2,\underline{b}}) A^l_{2,\underline{d}}\rangle\big]\end{aligned} \tag{5.5}$$

Recall that terms with an odd number of fields, e.g. $\sim \langle AAA\rangle$ have a vanishing expectation value. The expectation value then takes a form surprisingly similar to α^i:

$$\beta^i = -c_0 \left[\mu_2 \nabla^i \mu_1 - \mu_1 \nabla^i \mu_2\right] \,. \tag{5.6}$$

5.2 The Energy Momentum Tensor up to Order τ^3

The longitudinal flow of energy at order τ^2 can be calculated in the same way,

$$\begin{aligned}
\delta =&\langle [D^m, E_0][D^m, E_0] + [D^m, B_0][D^m, B_0]\rangle \\
=&g^2 f_{\underline{abe}} f_{\underline{cde}} \left(\delta^{ij}\delta^{kl} + \epsilon^{ij}\epsilon^{kl}\right) \left(\langle (\partial^m A^i)_{1,\underline{a}} (\partial^m A^k)_{1,\underline{c}}\rangle_{\rho_1} \langle A^j_{2,\underline{b}} A^l_{2,\underline{d}}\rangle_{\rho_2}\right. \\
&+ \langle A^i_{1,\underline{a}} A^k_{1,\underline{c}}\rangle_{\rho_1} \langle (\partial^m A^j)_{2,\underline{b}} (\partial^m A^l)_{2,\underline{d}}\rangle_{\rho_2} + \langle (\partial^m A^i)_{1,\underline{a}} A^k_{1,\underline{c}}\rangle_{\rho_1} \langle A^j_{2,\underline{b}} (\partial^m A)^l_{2,\underline{d}}\rangle_{\rho_2} \\
&+ \langle A^i_{1,\underline{a}} (\partial^m A^k)_{1,\underline{c}}\rangle_{\rho_1} \langle (\partial^m A)^j_{2,\underline{b}} A^l_{2,\underline{d}}\rangle_{\rho_2}) \\
&+ 2\frac{g^4}{2} f_{\underline{abA}} f_{\underline{eAB}} f_{\underline{cdC}} f_{\underline{fcB}} \left(\delta^{ij}\delta^{kl} + \epsilon^{ij}\epsilon^{kl}\right) \times \left(\langle A^m_{1,\underline{e}} A^m_{1,\underline{f}}\rangle_{\rho_1} \langle A^i_{1,\underline{a}} A^k_{1,\underline{c}}\rangle_{\rho_1} \langle A^j_{2,\underline{b}} A^l_{2,\underline{d}}\rangle_{\rho_2}\right. \\
&\left. + \langle A^i_{1,\underline{a}} A^k_{1,\underline{c}}\rangle_{\rho_1} \langle A^j_{2,\underline{b}} A^l_{2,\underline{d}}\rangle_{\rho_2} \langle A^m_{2,\underline{e}} A^m_{2,\underline{f}}\rangle_{\rho_2}\right) . \qquad (5.7)
\end{aligned}$$

Using formulas we derived in Chapter 4 Sec. 4.4, we have

$$\begin{aligned}
\delta =&4Q^2\epsilon_0 \ln^{-1}\frac{Q^2}{\hat{m}^2} \qquad (5.8)\\
&+ c_0\left[(\triangle\mu_1)\mu_2 + \nabla^i\mu_1\nabla^i\mu_2 + \mu_1(\triangle\mu_2)\right] \\
&+ \frac{g^4 N_c}{4\pi(N_c^2-1)} \ln\frac{Q^2}{\hat{m}^2}(\mu_1+\mu_2)\epsilon_0 .
\end{aligned}$$

Other new contributions to the energy momentum tensor at order τ^2 can be obtained by the same procedure,

$$\omega^i = \frac{(-1)^i}{2} c_0 \left[\partial^1\partial^1(\mu_1\mu_2) - \partial^2\partial^2(\mu_1\mu_2)\right] , \qquad (5.9)$$

$$\gamma = \frac{1}{2} c_0 \partial^1\partial^2(\mu_1\mu_2) . \qquad (5.10)$$

ω^i will break the isotropy of the pressure such that $T^{11} \neq T^{22}$.

The energy flow ξ^i at order τ^3 can be expressed as derivatives of second order

quantities. This has been proved explicitly in Eq. (3.30).

$$\xi^i = \nabla^i(-\triangle\epsilon_0 + \delta + \omega_i) - \nabla^j\gamma\,. \tag{5.11}$$

The rapidity odd flow at order τ^3 $\zeta^i = 0$ if we assume the correlator of three fields vanishes.

Hence after average the color configuration, the energy momentum tensor up to order $\mathcal{O}(\tau^3)$ in the (t, x, y, z) coordinates can be written as

$$T_{\rm f}^{\mu\nu} = \begin{pmatrix} T^{00}_{(0)} + \tau^2 T^{00}_{(2)} & \tau T^{01}_{(1)} + \tau^3 T^{01}_{(3)} & \tau T^{02}_{(1)} + \tau^3 T^{02}_{(3)} & T^{03}_{(0)} + \tau^2 T^{03}_{(2)} \\ \tau T^{01}_{(1)} + \tau^3 T^{01}_{(3)} & T^{11}_{(0)} + \tau^2 T^{11}_{(2)} & \tau^2 T^{12}_{(2)} & \tau T^{13}_{(1)} + \tau^3 T^{13}_{(3)} \\ \tau T^{02}_{(1)} + \tau^3 T^{02}_{(3)} & \tau^2 T^{12}_{(2)} & T^{22}_{(0)} + \tau^2 T^{22}_{(2)} & \tau T^{23}_{(1)} + \tau^3 T^{23}_{(3)} \\ T^{03}_{(0)} + \tau^2 T^{03}_{(2)} & \tau T^{13}_{(1)} + \tau^3 T^{13}_{(3)} & \tau T^{23}_{(1)} + \tau^3 T^{23}_{(3)} & T^{33}_{(0)} + \tau^2 T^{33}_{(2)} \end{pmatrix}. \tag{5.12}$$

Explicit expression can be obtained by combining the results of Chapters 3 and this Chapter. The full structure is too large to be listed here. For convenience, let us also give the energy momentum tensor up to order $\mathcal{O}(\tau^3)$ for brevity in the τ, x, y, η coordinate system. The metric tensor in that system is g^{mn} =diag$(1, -1, -1, -1/\tau^2)$. Then the energy momentum tensor can be written in a more compact form as

$$T_{\rm f}^{mn} = \begin{pmatrix} \epsilon_0 - \frac{\tau^2}{8}(-2\triangle\epsilon_0 + \delta) & \frac{\tau}{2}\alpha^x + \frac{\tau^3}{16}\xi^x & \frac{\tau}{2}\alpha^y + \frac{\tau^3}{16}\xi^y & \frac{\tau}{8}\nabla^i\beta^i \\ \frac{\tau}{2}\alpha^x + \frac{\tau^3}{16}\xi^x & \epsilon_0 - \frac{\tau^2}{4}(-\triangle\epsilon_0 + \delta + \omega_x) & \gamma & \frac{1}{2}\beta^x \\ \frac{\tau}{2}\alpha^y + \frac{\tau^3}{16}\xi^y & \gamma & \epsilon_0 - \frac{\tau^2}{4}(-\triangle\epsilon_0 + \delta + \omega_y) & \frac{1}{2}\beta^y \\ \frac{\tau}{8}\nabla^i\beta^i & \frac{1}{2}\beta^x & \frac{1}{2}\beta^y & -\frac{\epsilon_0}{\tau^2} + \frac{1}{8}(-2\triangle\epsilon_0 + 3\delta) \end{pmatrix}. \tag{5.13}$$

It is obvious that the energy momentum tensor is boost invariant since the components are independent of η in the τ, x, y, η coordinate system. This is a check that the original assumption of the MV model is intact. Eq. (5.13) and the detailed

expressions (5.2), (5.4) , (5.6), (5.9), (5.10) and (5.11) are one main result of this dissertation. The consequences of matching this energy momentum tensor to fluid dynamics will be discussed later.

5.3 An Electrodynamic Analogue

The rapidity-odd energy flow β^i is a surprising result. Traditionally boost-invariance in models of heavy ion collisions have led to only rapidity-even quantities. However, as we have already shown above, the energy momentum tensor (5.13) is explicitly boost-invariant despite the presence of β^i. Here we want to give an intuitive interpretation of the astonishing origin of such rapidity odd flow. Let us consider the following equivalent boundary value problem in classical electrodynamics. In the forward light cone $\tau > 0$ we have the Maxwell Equations $\partial_\mu F^{\mu\nu} = 0$ without sources. On the light cone $\tau = 0$ we demand the boundary conditions $\vec{E}(\tau = 0, \vec{r}) = E_0(\vec{r})\vec{e}_z$, $\vec{B}(\tau = 0, \vec{r}) = B_0(\vec{r})\vec{e}_z$, i.e. the initial fields are purely longitudinal. We also assume that those fields are related through transverse fields A_1^i and A_2^i as $E_0 = \delta^{ij} A_1^i A_2^j$ and $B_0 = \epsilon^{ij} A_1^i A_2^j$. The abelian problem for fixed initial conditions has been solved analytically in chapter 2 section 2.3, see also [62], but it will suffice here to give the solution order by order in powers of τ as we did in the case of QCD. From the QCD solutions we can immediately conclude that the longitudinal fields in the abelian case are

$$E^3 = \left(1 + \frac{t^2 - z^2}{4}\nabla^2\right) E_0 \tag{5.14}$$

$$B^3 = \left(1 + \frac{t^2 - z^2}{4}\nabla^2\right) B_0\,, \tag{5.15}$$

while the transverse fields are

$$E^i = \frac{z}{2}\nabla^i E_0 + \frac{t}{2}\epsilon^{ij}\nabla^j B_0 \tag{5.16}$$

$$B^i = \frac{z}{2}\nabla^i B_0 - \frac{t}{2}\epsilon^{ij}\nabla^j E_0\,, \tag{5.17}$$

for small times τ, i.e. $t^2 \approx z^2$. The Cartesian coordinates permit simple checks of these solutions with Gauss', Ampère's and Faraday's Laws.

There is a straight-forward interpretation of some aspects of these results. Let us choose, just as an example, a transverse position where $E_0, B_0 > 0$ and $\nabla^2 E_0$, $\nabla^2 B_0 < 0$ so that the longitudinal fields decrease away from the light cone $t^2 = z^2$. Two observers at fixed points $z = z_0 > 0$ and $z = -z_0$ would observe the same electric (magnetic) flux through a small transverse area a^2 with an initial value $E_0 a^2$ ($B_0 a^2$) at $t = z_0$ which then diminishes at the same rate $\nabla^2 E_0 a^2 t/2$ ($\nabla^2 B_0 a^2 t/2$) for both. Due to Ampère's (Faraday's) Law this reduction induces magnetic (electric) fields curling with a negative (positive) chirality around the longitudinal fields, respectively, see Fig. 5.1.

On the other hand the same two observers at fixed points z_0 and $-z_0$ can at time $t = z_0$ count the electric or magnetic flux through small cubes of volume a^3 whose sides are aligned with the coordinate axes. One side is held at $z = \pm z_0$, while the opposite side is at $z = \pm z_0 \mp a$ for the observer at z_0 or $-z_0$, respectively. In the former case the total flux out of the box due to the longitudinal field is $-z_0 a^3 \nabla^2 E_0/2 > 0$ while for the observer at $-z_0$ the net flux of longitudinal field has the opposite sign. Thus at z_0 a net flux of transverse field has to enter into the box while at $-z_0$ the same amount has to flow out of the box to satisfy Gauss' Law.

To summarize, the transverse fields naturally have a part due to Gauss' Law with vanishing circulation ($\epsilon^{ij}\nabla^j$), which is odd in η, and they have a part due to Ampère's

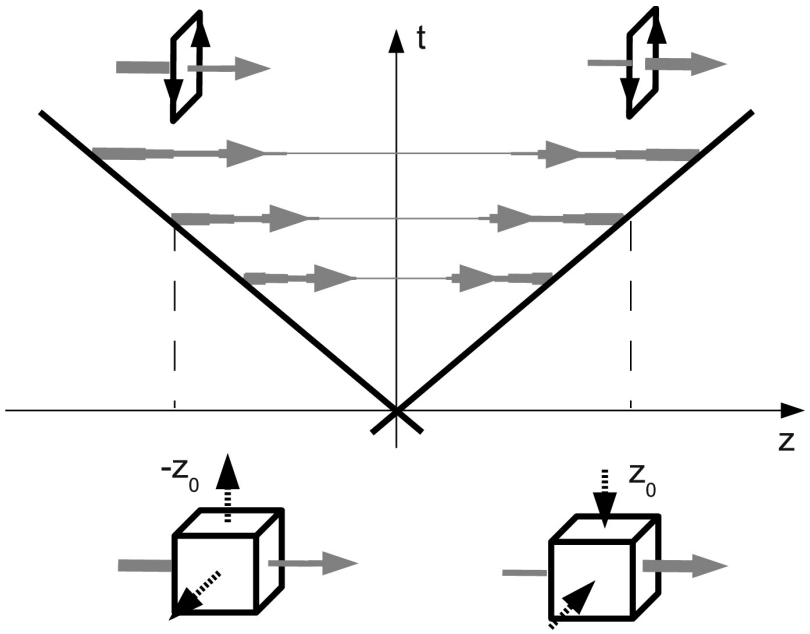

Figure 5.1: Two observers at $z = z_0$ and $z = -z_0$ test Ampère's and Faraday's Laws with areas a^2 in the transverse plane and Gauss' Law with a cube of volume a^3. The transverse fields from Ampère's and Faraday's Laws (black solid arrows) are the same in both cases, while the transverse fields from Gauss' Law (black dashed arrows) are observed with opposite signs. Initial longitudinal fields are indicated by solid grey arrows, thickness reflects field strength. Picture reprinted from [77] with permission from ELSEVIER.

and Faraday's Law (and with different signs between the magnetic and electric part due to the Lenz rule) with vanishing transverse divergence (∇^i), which is even in η. Fig. 5.2 shows the transverse electric and magnetic fields for two rapidities η for random fields A_1^i and A_2^i in a sector of the transverse plane. One can check that this statement about transverse fields translates directly into a matching statement about the transverse flow of energy since the initial transverse Poynting vector is linear in

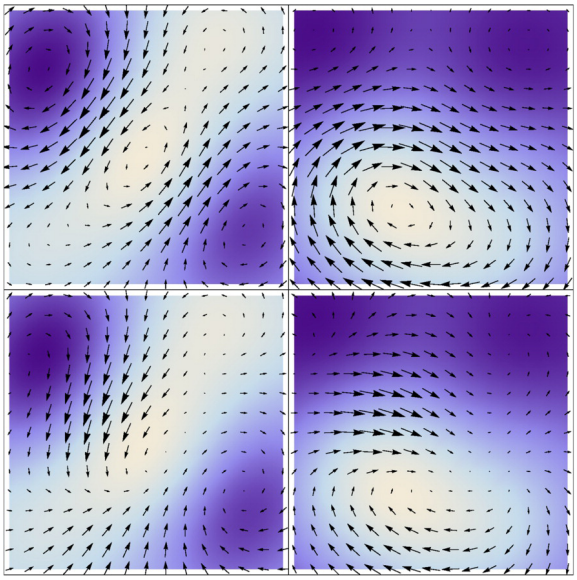

Figure 5.2: Transverse electric fields (left panels) and magnetic fields (right panels) at $\eta = 0$ (upper panels) and $\eta = 1$ (lower panels) in an abelian example for a random distribution of fields A_1^i, A_2^i. The initial longitudinal fields B_0 (left panels) and E_0 (right panels) are indicated through the density of the background (lighter color = larger values). At $\eta = 0$ the fields are divergence-free and clearly following Ampére's and Faraday's Laws, respectively. Picture reprinted from [77] with permission from ELSEVIER.

the transverse fields, $T^{0i} = \epsilon^{ij}(E^j B_0 - B^j E_0)$. Thus we have the four contributions already discussed in the case of QCD, two of them odd in η. Fig. 5.3 shows the flux of energy in the transverse plane for two rapidities for the same random configuration of fields A_1^i, A_2^i.

In order to make the connection between the electromagnetic analogue and QCD we note that the non-abelian terms at order $\mathcal{O}(\tau)$ contain odd numbers of fields which disappear upon averaging.

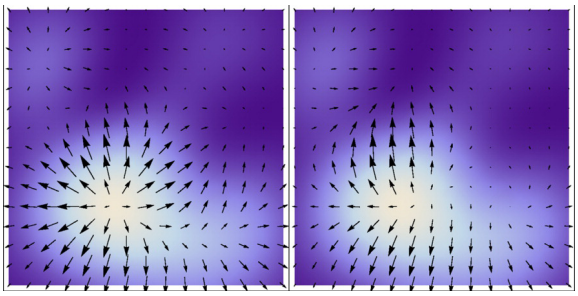

Figure 5.3: Example for transverse flow of energy for $\eta = 0$ (left panel) and $\eta = 1$ (right panel) in the abelian example for the same random distribution of fields A_1^i, A_2^i as in Fig. 5.2. The initial energy density T^{00} is shown through the density of the background (lighter color = larger values). At $\eta = 0$ the flow follows the gradient in the energy density in a hydro-like way while away from mid-rapidity energy flow gets quenched in some directions and amplified in others. Picture reprinted from [77] with permission from ELSEVIER.

5.4 Discussion of the Glasma Flow at $\mathcal{O}(\tau)$

Let us now explore some of the phenomenological consequences of color glass flow. The prediction of classical QCD for the initial average transverse energy flow normalized by the average initial energy density is

$$V^i = \frac{T^{0i}}{\epsilon_0} = -\frac{\tau}{2}\left(\cosh\eta \frac{\nabla^i(\mu_1\mu_2)}{\mu_1\mu_2} + \sinh\eta \frac{\mu_2\nabla^i\mu_1 - \mu_1\nabla^i\mu_2}{\mu_1\mu_2}\right) \tag{5.18}$$

which is independent of the UV cutoff Q and the IR m regulator. In the following we have calculated V^i in several situations using Woods-Saxon profiles for incident nuclei. Fig. 5.4 shows the average flow field V^i for the collision of two gold nuclei at impact parameter $b = 6$ fm in the transverse plane for two space-time rapidities.

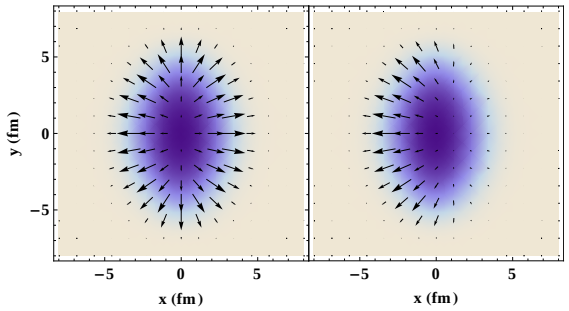

Figure 5.4: Flow field V^i (black arrows) and energy density ϵ_0 (shading) in the transverse plane for Au+Au collisions at $b = 6$ fm. The nucleus centered at $x = 3$ fm travels into the plane which is the positive η-direction. Left Panel: $\eta = 0$. Right Panel: $\eta = 1$. Picture reprinted from [77] with permission from ELSEVIER.

One can clearly see the evolution in rapidity from a hydro-like flow field at $\eta = 0$ to a preferred flow direction at forward rapidity.

In Fig. 5.5 the same collision is shown in the $\eta - x$-plane. Clearly the flow tilts the fireball clockwise. The orientation of rotation is as if the gluon flux tubes preferred to expand in the wake of spectator nucleons in such a way that the flow increases with increasing separation from the spectators in rapidity. However this can not be taken literally as the origin of the effect. Our calculation is based on a small time expansion and the response of the energy density to the flow will come in at the next order. Note that the normalization of the vector fields in the figures are arbitrary. Typical values of the flow V^i at the surface for Au+Au collisions are ~ 0.1 at $\tau = 0.1$ fm/c at midrapidity. Fig. 5.6 shows the average flow fields V^i for Au+Cu collisions at impact parameters $b = 0$ fm and $b = 2$ fm in the $\eta - x$-plane. In the central case the flow field leads to an expansion which is much more pronounced on the Cu-side of the system, consistent with the rule of thumb that flux tubes like to expand into the

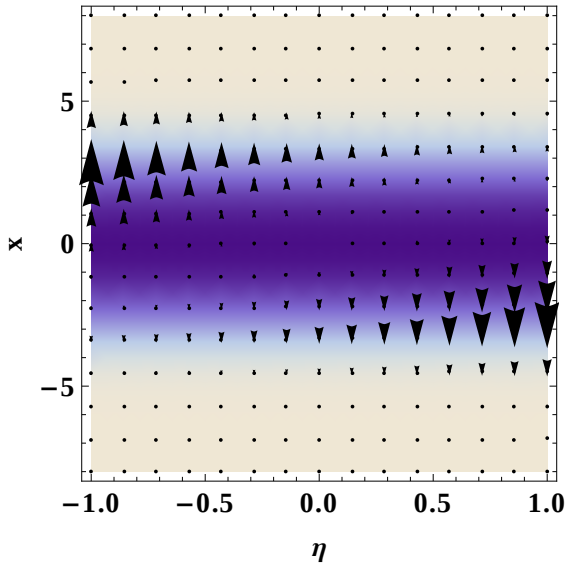

Figure 5.5: Same as Fig. 5.4 but plotted in the $\eta - x$-plane defined by $y = 0$. The flow will lead to a tilted fireball. Picture reprinted from [77] with permission from ELSEVIER.

wake of spectators (which here are solely from the gold nucleus). The flow pattern becomes more involved for Au+Cu collisions at finite impact parameter. In Fig. 5.7 the flow in the transverse plane is shown for forward and backward rapidity for the $b = 2$ fm Au+Cu system. We notice that the azimuthal modulation of the flow is non-trivial but can again be understood through the position of spectator nucleons from the Au nucleus (centered at $x = 1$ fm). This and the previous figures make it clear that $\vec{\beta}^i$ contributes not only to directed flow but also to the elliptic flow.

The flow of energy in the classical field before thermalization time $\tau_{\rm th}$ will translate into a flow of energy in the hydrodynamic phase after thermalization due to local energy and momentum conservation [67]. One expects remnants of this flow to survive in hydrodynamics due to the inertia of fluid cells and we will follow up this

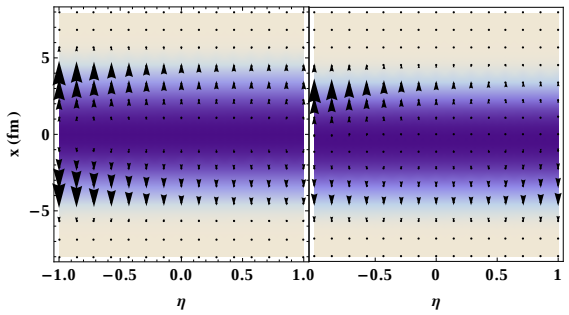

Figure 5.6: The same as Fig. 5.5 for Au+Cu (Au traveling to the right). Left Panel: $b = 0$ fm. Right Panel: $b = 2$ fm. Picture reprinted from [77] with permission from ELSEVIER.

idea in Chapter 7. In particular, this should result in a directed flow of particles which is odd in momentum rapidity y. In fact such a y-odd directed flow, measured by the first Fourier component v_1, has been observed at RHIC [81, 82, 83]. Fig. 5.8 shows experimental data for $v_1(\eta)$ of charged particles. The sign of the effect is consistent with the expectation from color glass, moreover the data points as a function of rapidity could be fitted with a $\sinh y$-shaped function. At this point it is too early to draw strong conclusions but the coincidence of sign and shape of the effect with data is encouraging.

Some of the qualitative features of the flow field discussed here have been generated in hydrodynamic simulations by initializing a tilted source [84], e.g. postulated in the fire streak model [85]. Our calculation suggests that color glass could account for this phenomenon without invoking additional model assumptions. In addition, classical QCD adds several unique predictions in particular for the case of collisions of asymmetric nuclei. A systematic study of flow as a function of rapidity and different nuclear systems could find this unique fingerprint of color glass.

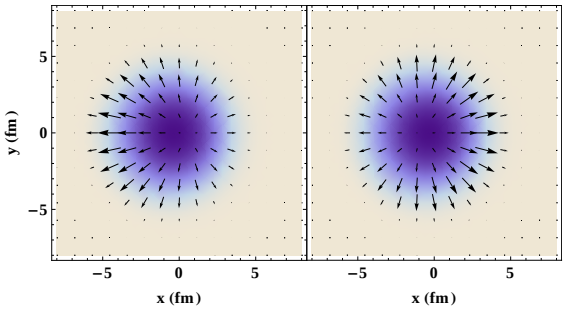

Figure 5.7: The same as Fig. 5.4 for Au+Cu at $b = 2$ fm. Left Panel: $\eta = 1$, Right Panel: $\eta = -1$. Picture reprinted from [77] with permission from ELSEVIER.

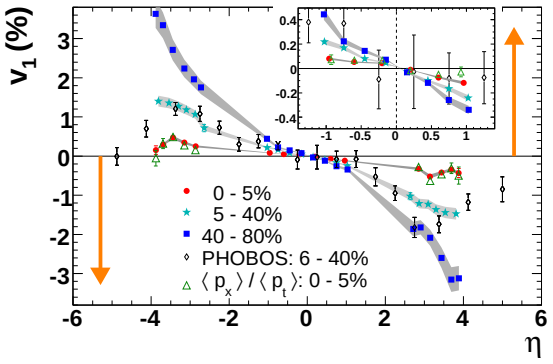

Figure 5.8: Experimental data for $v_1(\eta)$ of charged particles. Results for three centralities in Au+Au collisions at 200 GeV are shown. The direction of arrows indicate the algebraic sign of v_1 for spectator neutrons, and the positions of arrows on the η axis correspond to beam rapidity. The mid-η region is shown in more detail in the inset. The statistical errors are represented by error bars, and the shaded bands show systematic errors. Mid-central collisions results from PHOBOS [83] are also shown. Reprinted figure with permission from STAR Collaboration, Phys. Rev. Lett. 101, 252301 (2008) [81]. Copyright (2008) by the American Physical Society.

6. EVENT-BY-EVENT INITIAL CONDITIONS

In the previous chapter we calculated the energy momentum tensor averaged over all possible color configurations in nuclear collisions, which corresponds to the results coming from the average over many collisions. They can be compared to experimental data averaged over many events. We made the important discovery of rapidity-odd flow.

While traditionally observables averaged over many events have been the focus of attention, recently event-by-event analysis of heavy ion collisions have led to new discoveries like triangular flow v_3 [93]. Event-by-event analysis is critical for the study of physical quantities with large fluctuations around their mean values, or even theoreticaly vanishing mean value (like v_3). Consequently event-by-event initial conditions for hydrodynamics are desired. Only recently the first event-by-event color glass condensate calculation was presented by Schenke et al. [59]. However, the focus of that study was solely on the energy momentum density ϵ and flow was neglected. Here we would like to simulate the entire dynamics.

6.1 Gluon Fields of an Incoming Nucleus

We assume the color charges correlator satisfy the following relation, which is the discrete version of Eq. (4.3) ,

$$\langle \rho_{\underline{a}}(y_k^{\mp}, \vec{y}_{(i,j)}) \rho_{\underline{b}}(y_{k'}^{\mp}, \vec{y}_{(i',j')}) \rangle = \frac{g^2 \mu(\vec{y}_{(i,j)})}{N_{\mp}(N_c^2-1)} \delta_{\underline{ab}} \delta^{kk'} \delta^{ii'} \delta^{jj'} \tag{6.1}$$

where x_k and x'_k with $k, k' = 1, ..., N_{\mp}$ are the discrete $-$ or $+$ coordinates respectively, and $x_{(i,j)}$, $x_{(i',j')}$ with $i, i' = 1, ..., N_x$ and $j, j' = 1, ..., N_y$ are discrete coordinates on the transverse plane.

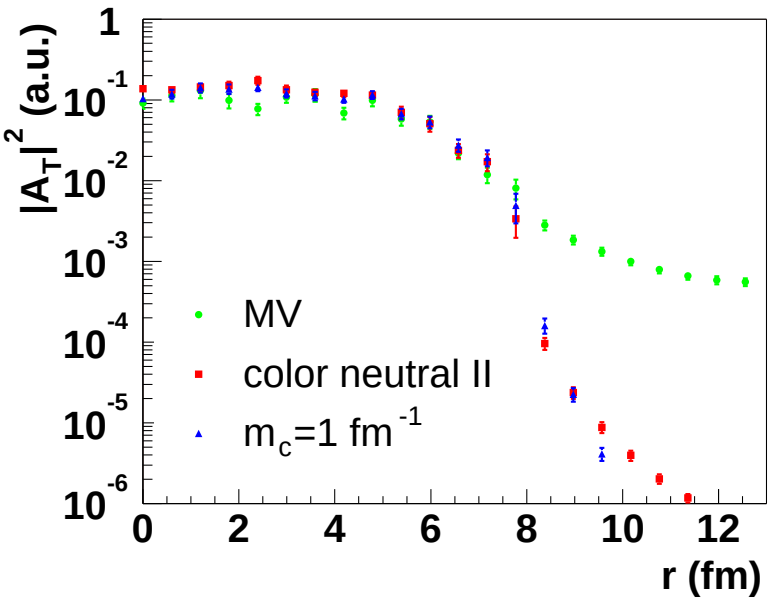

Figure 6.1: Gluon field as a function of radial distance calculated from the original MV model and a modified MV model with color neutrality constraints. The original MV model is shown by circles, while squares correspond to the Color Neutral II prescription in [87]. Results from Green's function with gluon mass 1 fm^{-1} are shown by triangles. Picture reprinted from [87] with permission from ELSEVIER.

For simplicity we assume

$$\mu(\vec{x}_\perp) = \mu_0 T_A(\vec{x}_\perp)\,, \tag{6.2}$$

where $\vec{x}_\perp$ is the transverse coordinate vector respect to the center of the nucleus, $T_A(\vec{x}_\perp) = \int_{-\infty}^{\infty} dz\, \kappa(\vec{r}_\perp)$ is a thickness function from the Woods-Saxon nuclear density profile $\kappa(\vec{r}_\perp)$, and μ_0 is the color charge squared per unit area in the center of each nucleus.

It has been point out by Lam and Mahlon [86] that a δ-function correlator of

color charges in the transverse plane as in Eq. (4.3) does not enforce color neutrality of the entire nucleus. In principal, a color neutrality condition should be imposed for consistency. However, Krasnitz et al. [87] showed that an IR regularization with a gluon mass effectively leads to confinement. They have checked that transverse gluon fields are almost the same with a gluon mass and with the color neutral condition imposed, see Fig.6.1. Since we impose a gluon mass m in our calculation color neutrality should be satisfied to good approximation in our calculation.

Let us recall from chapter 4 that the charge density ρ is assumed to be Gaussian distributed,

$$P[\rho] = \exp(-\int dx^- d^2\vec{x}_\perp \frac{\rho_{\underline{a}}(x^\mp, \vec{x}_\perp)\rho_{\underline{a}}(x^\mp, \vec{x}_\perp)}{2\mu(x^\mp, \vec{x}_\perp)}) \tag{6.3}$$

and that the Yang-Mills equations (2.1) with $\rho_{\rm cov}(x^-, \vec{x}_\perp)$ given for a single nucleus on the +-light cone in a covariant gauge reduces to the Laplace equation,

$$\Delta\alpha(x^-, \vec{x}_\perp) = -\rho_{\rm cov}(x^-, \vec{x}_\perp) \tag{6.4}$$

for where $A^\mu_{\rm cov} = \delta^{\mu+}\alpha$. The explicit solution is,

$$\alpha(x^-, \vec{x}_\perp) = \int dz^2_\perp G(\vec{x}_\perp - z_\perp)\rho_{\rm cov}(x^-, \vec{z}_\perp) \tag{6.5}$$

where the Green's function is given by its Fourier transformed counterpart $\tilde{G}(k) = 1/(k^2 + m^2)$.

Now we describe the numerical implementation of these equations. First we simulate a random distribution of the charge density in x^- and $\vec{x}_\perp$ (indexed by (k,i,j)) given by the probability distribution (6.3). Then we use fast Fourier transformation in the two transverse coordinates to obtain $\tilde{\rho}_{cov,\underline{a}}(x^-_k, \vec{k}_{(i,j)})$. The convolution (6.5)

then becomes a simple product,

$$\tilde{\alpha}_{\underline{a}}(x_k^-, \vec{k}_{(i,j)}) = \tilde{\rho}_{cov,\underline{a}}(x_k^-, \vec{k}_{(i,j)}) \times \tilde{G}(\vec{k}_{(i,j)})\,. \tag{6.6}$$

An inverse Fourier transformation then will give us the $\alpha_{\underline{a}}(x_k^-, \vec{x}_{i,j})$ on the space time lattice site.

The gluon field A^i in light cone gauge can be derived from the covariant expression with the help of the Wilson line

$$U(x^-, x_\perp) = \mathcal{P} \exp\left[-ig \int_{-\infty}^{x^-} \alpha(z^-, \vec{x}_\perp) dz^-\right]. \tag{6.7}$$

Here $\mathcal{P}$ denotes path ordering of the fields α from right to left. The discrete form of path integral then can be written as [89],

$$U(x_{(i,j)}) = \prod_{k=1}^{N_-} \exp\left[-ig\alpha_{\underline{a}}(x_k^-, \vec{x}_{i,j})\right]\,. \tag{6.8}$$

Recall that x_k^- are the grid sites along the x^- coordinate. The pure gauges at the site (i,j) are defined on the lattice as

$$V^m(\vec{x}_{(i,j)}) = U(\vec{x}_{(i,j)}) U^\dagger(\vec{x}_{(i,j)} + \hat{e}_m), \quad (m = 1, 2)\,. \tag{6.9}$$

While the gluon fields $A^m(\vec{x}_{(i,j)})$ are related to $V^m(\vec{x}_{(i,j)})$ by,

$$V^m(\vec{x}_{(i,j)}) = \exp[igaA^m(\vec{x}_{(i,j)})], \quad (m = 1, 2)\,. \tag{6.10}$$

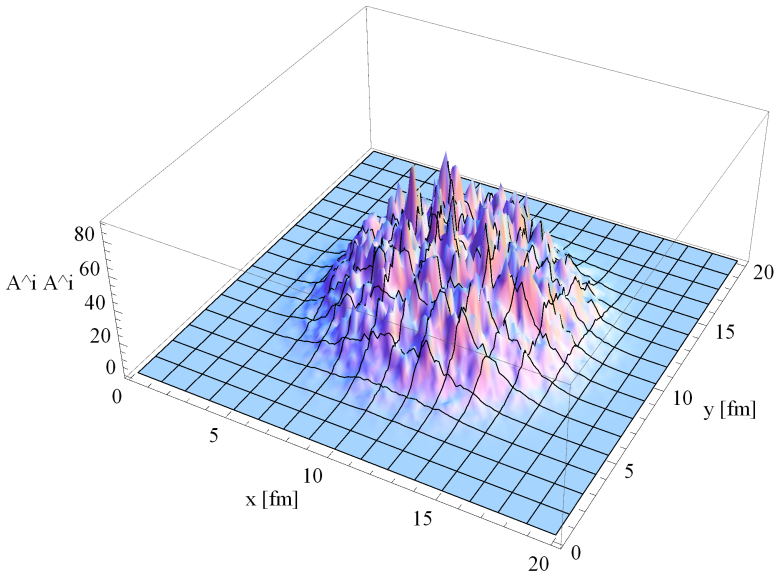

Figure 6.2: A typical gluon distribution $A^i A^i$ in the transverse plane.

6.2 Gluon Correlator from One Event

Following the procedure described in the last section, we simulate the charge distribution of two nuclei on a 10×10 fm transverse square with a 0.02 fm grid and 10 grid points in longitudinal direction. The convolution is done using a Fast Fourier Transformation (FFT) code. The gauge transformations Eq. (6.7) on each lattice site is then determined. The initial gluon fields on both nuclei can thus be easily obtained using Eq. (6.10). Fig. 6.2 shows the gluon distribution function $A^i_{\underline{a}} A^i_{\underline{a}}$ of one nucleus in the transverse plane. In order to make sure our simulation is consistent with the original prediction of the MV model, we simulate many events and average the results for the gluon distribution function to obtain $\langle A^i A^i \rangle_{E-by-E}$. A comparison of one simulation, the event averaged $\langle A^i A^i \rangle_{E-by-E}$ simulation and the prediction $\langle A^i A^i \rangle$ of the original MV model (see Eq. (4.37)) are shown in Fig. 6.3. We make two important observations. First, the event-by-event average and the analytic average

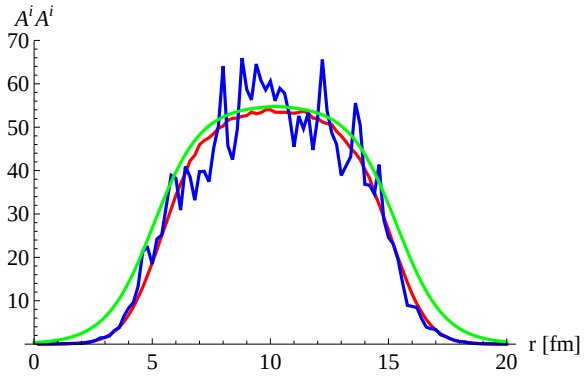

Figure 6.3: A plot of the gluon correlator A^iA^i in light cone gauge. Along a line through the center of a gold nucleus, the average distribution simulated, predicted by the original MV model (green line), from the simulation of one typical configuration (note: this is not a particular nucleus; it would change with time!) (blue line) and the average over 500 configuration (red line) are shown.

agree well. Residual deviations might be the effect of different implementations of IR and UV cutoffs in both calculations. Second, we note that fluctuations in single events are sizable but not dominant. Thus the analytic, averaged results from the previous chapter will play an important role in single events as well.

6.3 Physical Observables from Numerical Simulations

After the acquisition of the gluon distribution, the components of the energy momentum tensor then can be calculated using the formulas we derived in Chapter 5. The energy density from one typical event with impact parameter $b = 6$ fm is shown in Fig. 6.4. It exhibits strong fluctuations compare to the previous averaged results. Such fluctuations may have significant influences on final observables, e.g. jet quenching [88] and odd terms of flow. A comparison of the initial energy density ϵ_0 of random event, the average over many events and the prediction of the original

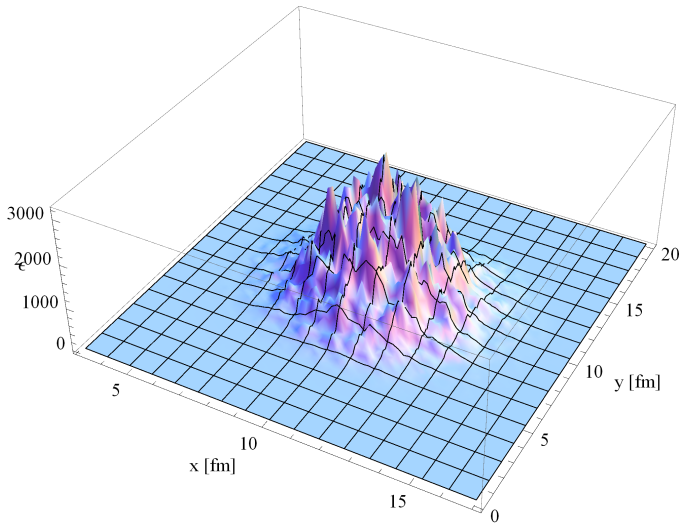

Figure 6.4: Energy density of one event of colliding gold nuclei from the above procedure, b=6 fm, arbitrary scale on the vertical axis.

MV model is shown in Fig. 6.5.

The transverse flow can also be calculated event by event. Fig. 6.6 shows the hydro-like flow $\vec{\alpha}$ for the same event as in Fig. 6.4 and an event averaged $\vec{\alpha}$. We quantify the net effect of $\vec{\alpha}$ by calculating a dimensionless quantity

$$\langle \alpha \rangle = \int \frac{d^2\vec{r}}{r} \frac{\vec{\alpha}(\vec{r})}{\epsilon_0(\vec{r})} \cdot \frac{\vec{r}}{|r|} , \tag{6.11}$$

which is the radial component of the energy flow per energy density averaged over the transverse plane. The prediction by the original MV model for $b = 6$ fm is $\langle \alpha \rangle_{MV} = 52.226$. $\langle \alpha \rangle$ calculated by averaging over 500 events is $\langle \alpha \rangle_{E-by-E} = 99.88$ for matching integration domains in the transverse plane. We also can define a

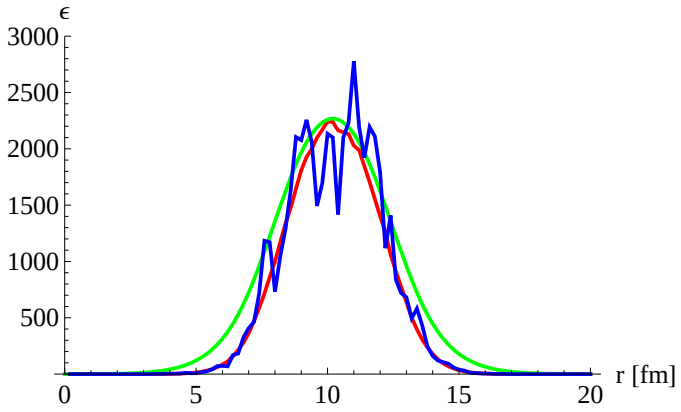

Figure 6.5: A plot of the energy density ϵ_0 in Au+Au collisions along the direction of the impact vector (collision center located at 10 fm). Energy densities predicted by the original MV model (green line), from simulation of one event (blue line) and the averaged over 500 events (red line) are shown respectively.

measure of the initial elliptic flow as,

$$\langle Q \rangle = \int \frac{d^2\vec{r}}{r} \frac{\vec{\alpha}(\vec{r})}{\epsilon_0(\vec{r}\cos(2\phi))} \cdot \frac{\vec{r}}{|r|}\,, \tag{6.12}$$

where ϕ is the azimuthal angle. We have $\langle Q \rangle_{MV} = -11.22$ in the original MV model and $\langle Q \rangle_{E-by-E} = -20.80$ after averaging over 500 events.

Fig. 6.7 shows the η-odd flow component $\vec{\beta}$ simulation of the same single event as before and the event-averaged $\vec{\beta}$. We can also quantify the net effect of β by calculating a dimensionless quantity

$$\langle \beta \rangle = \int \frac{d^2\vec{r}}{r} \frac{\vec{\beta} \cdot \hat{e}_x}{\epsilon_0(\vec{r})}\,, \tag{6.13}$$

which integrates the flow component along the impact vector per energy density.

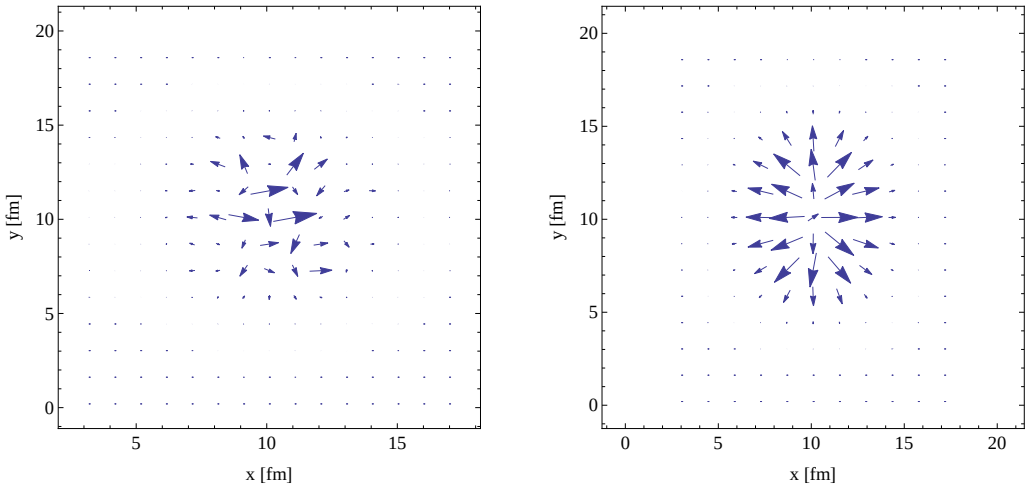

Figure 6.6: Hydro-like flow component $\vec{\alpha}$ from simulation of one event (left) and averaged $\vec{\alpha}$ of 500 simulations (right) respectively.

The prediction by the original MV model for $b = 6$ fm is $\langle\beta\rangle_{MV} = -29.9$. $\langle\beta\rangle$ calculated by averaging over 500 events is $\langle\beta\rangle_{E-by-E} = -57.42$. The event-by-event average gives larger flow than the original MV model prediction. The reason could be the original MV model, with the charge distribution totally uncorrelated in the transverse plane, is corresponding to setting $m \to 0$ in numerical simulation. If we use the charge distribution proposed by Lam and Mahlon [86], the value of $\langle\alpha\rangle$, $\langle\beta\rangle$ and $\langle Q\rangle$ then are comparable to our numerical simulation. In the future a more thorough study is required to understand how average flow effects emerge from event-by-event flow fields.

The discussion above leads to the conclusion that our numerical simulation can provide the correct energy momentum tensor of glasma fields for single nuclear collisions. The results reproduce the original MV model predictions if we average over a large enough number of events. We emphasize that for the first time a simulation of

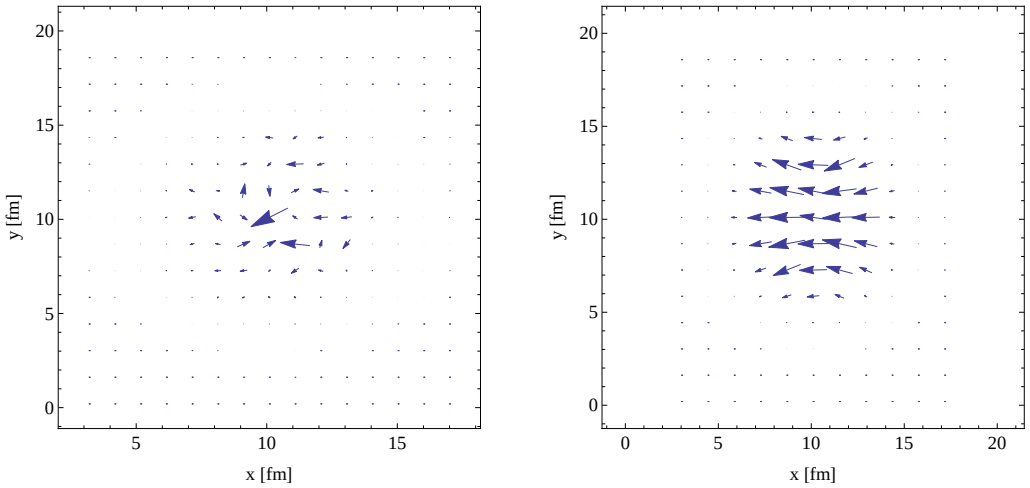

Figure 6.7: The η-odd flow component $\vec{\beta}$ from simulation of one event (left) and event-averaged $\vec{\beta}$ of 500 simulations (right) respectively.

collisions on an event-by-event basis will give fluctuations of the energy density and the flow profile at the same time. Higher order terms in τ results can be obtained similarly but we skip details for brevity. In principal, nucleon position fluctuations can be implemented on top of the Woods-Saxon profile, Eq. (6.2) using the same procedure for more realistic results.

7. FROM GLASMA TO PLASMA

In order to make comparison with experimental data, we need a model to translate the flow of glasma into flow of final particles observed by the detector. From experimental data we have learned that the matter produced in heavy ion collisions thermalizes very early, at a time scale < 1 fm/c [40]. The classical Yang-Mills equations do not predict thermalization. However the phenomenology is clear: the classical gluon field has to decay into quarks and gluons in chemical equilibrium and those particles have to equilibrate. There have been attempts in the literature to model this process [43]. Here we simply extract information about thermalized plasma from the energy momentum tensor of the glasma. We assume a very rapid thermalization, from which we can derive matching conditions for ideal hydrodynamics analytically. A matching to viscous hydrodynamics initial conditions can also be derived. We then discuss some of the phenomenological consequences, which include a tilted fireball which has the potential to explain the directed flow observed at RHIC. Preliminary results of a further 3+1 D viscous hydrodynamic evolution from such initial conditions are presented as well.

7.1 Matching to Ideal Hydrodynamics

The energy momentum tensor T_{ideal} of an ideal fluid in the lab frame is given by its local energy density e, pressure p and the 4-velocity u^μ of the fluid,

$$T^{\mu\nu}_{ideal} = (e+p)u^\mu u^\nu - pg^{\mu\nu} \tag{7.1}$$

We assume instantaneous thermalization from glasma to plasma at thermalization time τ_{th}, so the energy momentum tensor has the following structure in τ, first

proposed in [60],

$$T^{\mu\nu} = \Theta(\tau_{th} - \tau)T_f^{\mu\nu} + \Theta(\tau - \tau_{th})T_{pl}^{\mu\nu} \,. \tag{7.2}$$

Where $T_f^{\mu\nu}$ is the energy momentum tensor of the gluon field and $T_{pl}^{\mu\nu}$ is its counterpart for quark gluon plasma. In this section we assume $T_{pl}^{\mu\nu} = T_{ideal}^{\mu\nu}$. Whatever the microscopic mechanism for gluon fields to decay into plasma, energy and momentum should be conserved, i.e. $\partial_\mu T^{\mu\nu} = 0$. This gives us four equations connecting $T_f^{\mu\nu}$ and $T_{pl}^{\mu\nu}$. Together with the equation of state (EOS) $p(e)$, we have enough equations to solve for e, pressure p and fluid velocity.

Using the parametrization of $T_f^{\mu\nu}$ from Eq. (5.13), we can find the following analytic solution from energy momentum conservation [60, 92],

$$\begin{aligned}
\vec{v}_\perp =& \frac{1}{\cosh\eta} \frac{\vec{\alpha}}{\epsilon_0 - \frac{\tau_{th}^2}{8}(-2\triangle\epsilon_0 + \delta) + p}, \\
v_L =& \tanh\eta, \\
e + p =& (\epsilon_0 - \frac{\tau_{th}^2}{8}(-2\triangle\epsilon_0 + \delta) + p)\left(1 - \frac{\vec{\alpha}^2}{(\epsilon_0 - \frac{\tau_{th}^2}{8}(-2\triangle\epsilon_0 + \delta) + p)^2}\right) .
\end{aligned} \tag{7.3}$$

Here e is the local energy density of the fluid and ϵ_0 is the energy density of the gluon fields at $\tau = 0$ as defined in (3.2).

It is interesting to note that even though we do not require the hydrodynamic fluid to be boost-invariant at the outset, the matching of a ideal hydrodynamic fluid to the initial fields automatically gives boost-invariant results. We note two shortcomings of the matching to ideal hydrodynamics. First, one can check that individual components of $T^{\mu\nu}$ can be non-continuous at τ_{th}. This clearly is an artifact of the 4 matching equations not doing justice to the ten degrees of freedom of the

energy momentum tensor. Secondly, the space time rapidity-odd flow $\vec{\beta}$ we discussed in Chapter 5 does not enter at all. It will turn out this is due to our requirement that only energy and momentum be conserved while $\vec{\beta}$ is related to a tilting of the fireball and thus angular momentum in the system. This leads to the idea to also impose angular momentum conservation.

7.2 Matching to Viscous Hydrodynamics

Clearly angular momentum should also be conserved during thermalization. A 3-rank angular momentum density tensor can be introduced to deal with angular momentum conservation of fields,

$$\mathcal{M}^{\mu\nu\rho} = x^{\mu}T^{\nu\rho} - x^{\nu}T^{\mu\rho} \tag{7.4}$$

If we set $\rho = 0$ we can have an antisymmetric tensor,

$$M^{\mu\nu} = \int d^3\vec{x}\mathcal{M}^{\mu\nu 0} \tag{7.5}$$

It is easy to check that $M^{\mu\nu} = \epsilon^{ijk}L_k$, where L_k is the usual angular momentum operator and ϵ^{ijk} is the Levi-Civita symbol.

We require that the total angular momentum density tensor

$$\mathcal{M}^{\mu\nu\rho} = \Theta(\tau_0 - \tau)\mathcal{M}_f^{\mu\nu\rho} + \Theta(\tau - \tau_0)\mathcal{M}_{pl}^{\mu\nu\rho} \tag{7.6}$$

is conserved such that,

$$\partial_{\rho}\mathcal{M}^{\mu\nu\rho} = 0\,. \tag{7.7}$$

Eq. (7.7) together with $\partial_{\mu}T^{\mu\nu} = 0$ and the equation of state, give us ten independent

equations. It turns out that the number of equations and the number of degrees of freedom in the viscous hydrodynamic energy momentum are the same at ten and thus a component by component match between $T_f^{\mu\nu}$ and $T_{pl}^{\mu\nu}$ is the natural solution. We recall the most general form of the energy momentum tensor is,

$$T_{viscous}^{\mu\nu} = (e + p + \Pi)u^\mu u^\nu - (p + \Pi)g^{\mu\nu} + \pi^{\mu\nu} \,. \tag{7.8}$$

Where $\pi^{\mu\nu}$ is the shear stress tensor and Π is the bulk stress as discussed in Chapter 1. The shear stress tensor $\pi^{\mu\nu}$ must be traceless, symmetric and also orthogonal to the 4-velocity of the fluid,

$$u_\mu \pi^{\mu\nu} = 0 = \pi^{\mu\nu} u_\mu \,, \tag{7.9}$$

so it only has five independent components. e , u^μ and Π give us five more quantities to be determined in the matching. Note that the energy momentum tensor $T_f^{\mu\nu}$ is always traceless by construction, while $T_{pl}^{\mu\nu}$ can have non-vanishing trace for a realistic equation of state and bulk stress tensor. It turns out that the matching will only determine the combination $p + \Pi$ and the equation of state will separate equilibrium pressure and bulk stress.

We can choose five independent components for $\pi^{\mu\nu}$ arbitrarily, but we found it is convenient to work with π^{11},π^{12},π^{13},π^{22} and π^{23} as independent components. The

other components then can be written down as,

$$\begin{aligned}
\pi^{00} =&(\pi^{11}v_x^2 + 2\pi^{12}v_xv_y + 2\pi^{13}v_xv_z + \pi^{22}v_y^2 + 2\pi^{23}v_yv_z \\
&- \pi^{11}v_z^2 - \pi^{22}v_z^2)/(1-v_z^2)\,, \\
\pi^{01} =&\pi^{11}v_x + \pi^{12}v_y + \pi^{13}v_z\,, \\
\pi^{02} =&\pi^{12}v_x + \pi^{22}v_y + \pi^{23}v_z\,, \\
\pi^{03} =&(\pi^{11}v_x^2v_z + \pi^{13}v_x + 2\pi^{12}v_xv_yv_z + \pi^{13}v_xv_z^2 + \pi^{22}v_y^2v_z + \pi^{23}v_y \\
&+ \pi^{23}v_yv_z^2 - \pi^{11}v_z - \pi^{22}v_z)/(1-v_z^2)\,, \\
\pi^{33} =&\pi^{00} - \pi^{11} - \pi^{22}\,,
\end{aligned} \tag{7.10}$$

due to the orthogonality condition (7.9) and traceless condition. Next we will discuss some analytical solution at special positions in the fireball to interpret some basic properties of matching to a viscous hydrodynamics fluid assuming instantaneous thermalization. Then a numerical solution for the entire fireball will be presented.

7.2.1 Analytical Solution at the Center

Let us match the viscous plasma tensor to a 1^{st} order in time gluon field energy momentum tensor at time τ_{th} in order to study the effect of $\vec{\beta}$, which was missing in ideal hydrodynamics. Keep in mind that at the center $\alpha^x = 0$, $\alpha^y = 0$ and $\beta^y = 0$, i.e.

$$T^{\mu\nu}_{\rm f} = \begin{pmatrix} \epsilon_0 & \frac{\tau_{th}}{2}\beta^x \sinh\eta & 0 & 0 \\ \frac{\tau_{th}}{2}\beta^x \sinh\eta & \epsilon_0 & 0 & \frac{\tau_{th}}{2}\beta^x \cosh\eta \\ 0 & 0 & \epsilon_0 & 0 \\ 0 & \frac{\tau_{th}}{2}\beta^x \cosh\eta & 0 & -\epsilon_0 \end{pmatrix}. \tag{7.11}$$

There is an analytical solution,

$$
\begin{aligned}
& e = \epsilon_0, \quad (p + \Pi) = \frac{1}{3}\epsilon_0, \quad v_x = v_y = 0, \quad v_z = \tanh\eta \\
& \pi^{11} = \pi^{22} = \frac{2}{3}\epsilon_0, \quad \pi^{13} = \frac{\tau_{th}}{2}\beta^x \cosh\eta, \quad \pi^{01} = \frac{\tau_{th}}{2}\beta^x \sinh\eta\,.
\end{aligned} \tag{7.12}
$$

There are a few features we can conclude from the above analytical solution. First, $\pi^{33} = -\frac{4}{3}\epsilon_0$. Hence the negative longitudinal pressure in $T_f^{\mu\nu}$ will result in shear stress components at the order of the equilibrium pressure p. Practically the effective longitudinal pressure should be positive at time of thermalization. However, without detailed knowledge of the thermalization mechanism, we rely on viscous hydrodynamics to relax the far off-equilibrium bulk and shear stress toward their Navier-Stokes values for further approach to equilibrium. We also note that interestingly the rapidity-odd flow $\vec{\beta}$ translates into viscous energy and momentum flow π^{01}, π^{13} etc. We expect the hydrodynamic evolution to relax those shear components to their Navier-Stokes values and thereby to shift the corresponding flow to the velocity field u^μ.

7.2.2 Numerical Solutions

It is not clear that the set of ten independent non-linear equations from the matching always have analytical solutions, in particular if we match to more complicated tensors $T_{\rm f}^{\mu\nu}$ beyond 1^{st} order in time. One option is a non-linear equations solving algorithm such as Newton-Raphson and we have developed a code based on this method. There is also an elegant method to turn the matching to a eigenvalue problem.

It is obvious, that if a ideal fluid is moving with 4-velocity

$$u^\mu = \gamma(1, v_x, v_y, v_z), \tag{7.13}$$

where γ is the Lorentz factor $\gamma = 1/\sqrt{1 - v_x^2 - v_y^2 - v_z^2}$, we should have,

$$\Big((e + p)u^\mu u^\nu - p g^{\mu\nu}\Big)u_\nu = e u^\mu \,. \tag{7.14}$$

On the other hand, the shear stress tensor should be orthogonal to the 4-velocity, $\pi^{\mu\nu}u_\nu = 0$. As a result, for any given total energy momentum tensor of a viscous hydrodynamic fluid, it must have an eigenvalue and corresponding eigenvector such that,

$$T^{\mu\nu}_{viscous} u_\nu = e u^\mu \,. \tag{7.15}$$

Thus we can find the energy density and 4-velocity by diagonalizing the energy momentum tensor of the fields $T^\mu_{\mathrm{f},\nu}(\tau_{th}, \vec{x}, \eta)$ and selecting the eigenvector which must be time-like in Minkowski space. This works as long as the eigenvalues are not degenerate. The eigenvalues for the field energy momentum tensor including only τ^0 and τ^1 terms,

$$T^{\mu\nu}_{\mathrm{f}} = \begin{pmatrix} \epsilon_0 & \frac{\tau_{th}}{2}(\alpha^x \cosh\eta + \beta^x \sinh\eta) & \frac{\tau_{th}}{2}(\alpha^y \cosh\eta + \beta^y \sinh\eta) & 0 \\ \frac{\tau_{th}}{2}(\alpha^x \cosh\eta + \beta^x \sinh\eta) & \epsilon_0 & 0 & \frac{\tau_{th}}{2}(\alpha^x \sinh\eta + \beta^x \cos\eta) \\ \frac{\tau_{th}}{2}(\alpha^y \cosh\eta + \beta^y \sinh\eta) & 0 & \epsilon_0 & \frac{\tau_{th}}{2}(\alpha^y \sinh\eta + \beta^y \cos\eta) \\ 0 & \frac{\tau_{th}}{2}(\alpha^x \sinh\eta + \beta^x \cos\eta) & \frac{\tau_{th}}{2}(\alpha^y \sinh\eta + \beta^y \cos\eta) & -\epsilon_0 \end{pmatrix}, \tag{7.16}$$

can be found analytically and the eigenvalues are generally not degenerate. The expressions for the eigenvalues are too lengthy to be shown. In the special case, $\alpha^y =$

$\beta^y = 0$, the eigenvalues are ϵ_0, $-\epsilon_0$, $\sqrt{\epsilon_0^2 + (\beta^x)^2 - (\alpha^x)^2}$ and $-\sqrt{\epsilon_0^2 + (\beta^x)^2 - (\alpha^x)^2}$ and they are not degenerate. Hence except under some very rare circumstances, the eigenvalue method can uniquely determine the energy density and 4-velocity of the viscous fluid. The shear stress tensor then immediately follows by subtracting the ideal part from the energy momentum tensor of the fields. Keep in mind that the physical eigenvalue must be positive, and the physical eigenvector must be a time like vector.

For more complicated tensors $T^{\mu}_{\mathrm{f},\nu}(\tau_{th}, \vec{x}, \eta)$ we employ the QR algorithm [90] to find the eigenvalues and eigenvectors of the energy momentum tensor numerically. We have created viscous hydrodynamic initial conditions for $T^{\mu\nu}_{\mathrm{f}}$ up to second order in time. The most surprising results of viscous matching (and thus taking into account $\vec{\beta}$) is a tilting of the fireball in the direction of $\vec{\beta}$. Of course this should not really be surprising given the nature of the flow field $\vec{\beta}$.

7.3 Results from Matching

Here we show some results for viscous matching using $\mathcal{O}(\tau^2)$ gluon fields in the x-η plane at $y = 0$ to illustrate how the viscous hydrodynamics fields are tilted. Fig. 7.1 shows the longitudinal velocity $v_z = 0$ in the x-η plane at $y = 0$. At $x = 0$, $v_z = \tanh\eta$. We observe that the node line for which $v_z = 0$ moves away from $x = 0$, representing a rotation of the $v_z = 0$ node line. At transverse position $x = 5$ fm, the position of $v_z = 0$ is shifted to $\eta \approx 0.4$, which gives quite a strong tilting effect.

Fig. 7.2 shows the transverse velocity field v_x in the x-η plane at $y = 0$. We recall that the hydro-like flow has a dominate $\sim \frac{1}{\cosh\eta}$ dependence at $x = 0$ (see Eq. (7.3)) and an increase with increasing radial gradient, i.e. toward larger $|x|$. However in addition we notice that the transverse velocity field v_x exhibits the same tilting effects as the v_z field. The shear stress tensor π^{01} in the x-η plane at $y = 0$

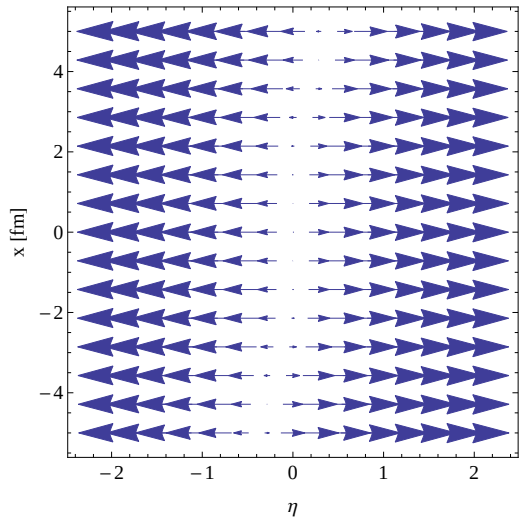

Figure 7.1: Longitudinal velocity v_z in the x-η plane at $y = 0$. Note that the node line for $v_z = 0$ is tilted away from $\eta = 0$.

is determined by $\vec{\beta}$ and shows an unaumbigous pattern of tilting. We expect that in a hydrodynamic evolution, π^{01} will eventually relax to its Navier-Stokes value and a rapid-odd transverse flow in x will be built up instead. We will see this happen in the next section.

7.4 Preliminary Results from Viscous Hydrodynamics Evolution

A (3+1)D viscous hydrodynamic code is currently being developed by S. Somanathan [91], but is not part of this dissertation. Preliminary results from this code using the initial conditions from the last section have confirmed that a rapidity-odd flow pattern emerges that could explain the directed flow observed in RHIC. At this time, we can not calculate spectra of particles as the hydrodynamic code does not have a freeze-out module yet. A simple ideal gas EOS $e = 3p$ has been used in this calculation.

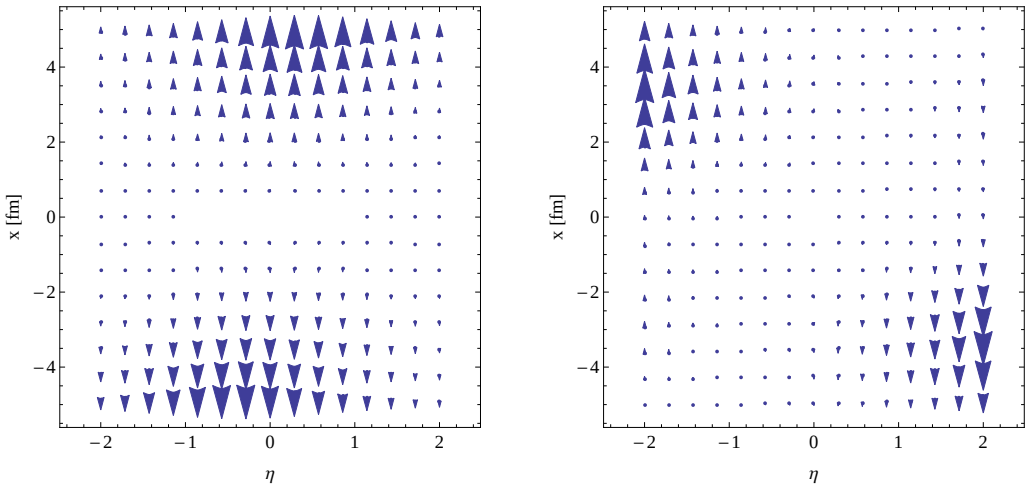

Figure 7.2: Left: Transverse velocity v_x in the x-η plane at $y = 0$. Right: Shear stress tensor π^{01} in the x-η plane at $y = 0$. It shows a pattern of tilting.

Fig. 7.3 shows the energy density and the shear stress component π^{11} averaged over transverse coordinates at thermalization time $\tau_{th} = 0.2$ fm (blue line) and at 0.8 fm (red line) after viscous hydrodynamic evolution. π^{11} decreases very fast towards its Navier-Stokes value. π^{22} and π^{33} behave similarly to π^{11}.

Fig. 7.4 shows the shear stress π^{13} averaged over transverse coordinates at thermalization time $\tau_{th} = 0.2$ fm (blue line) and at 0.8 fm (red line) after viscous hydrodynamic evolution. Shear stress components π^{01} and π^{03} also decrease very fast towards their Navier-Stokes values. A finite η-odd effective transverse velocity v_x develops from the decrease of the shear stress tensor as expected. Fig 7.5 shows the fluid velocities v_x and v_y averaged over transverse coordinates as functions of η at thermalization time $\tau_{th} = 0.2$ fm (blue line) and at 0.8 fm (red line) after viscous hydrodynamic evolution. Thus indeed the η-odd flow of glasma has been translated to a η-odd flow in hydrodynamics.

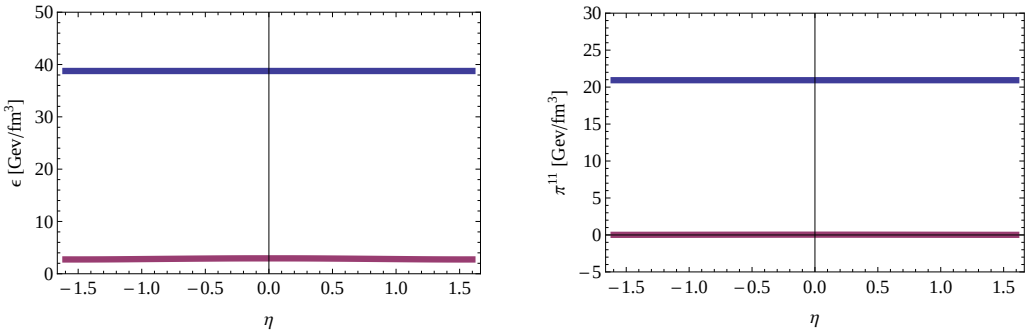

Figure 7.3: Left: The energy density averaged over transverse coordinates as a function of η at thermalization time $\tau_{th} = 0.2$ fm (blue line) and at 0.8 fm (red line) after viscous hydrodynamic evolution. Right: The shear stress π^{11} averaged over transverse coordinates at thermalization time $\tau_{th} = 0.2$ fm (blue line) and at 0.8 fm (red line) after viscous hydrodynamic evolution.

To summarize, our results show that the η-odd flow of the glasma we calculated from the CGC will indeed result in a *tilted* hydrodynamic fireball with a rapidity-odd flow component. We expect it to contribute, among other sources, to the directed flow observed in RHIC [81]. We plan to perform a thorough study when the viscous hydrodynamic code with realistic EOS and freeze-out is available.

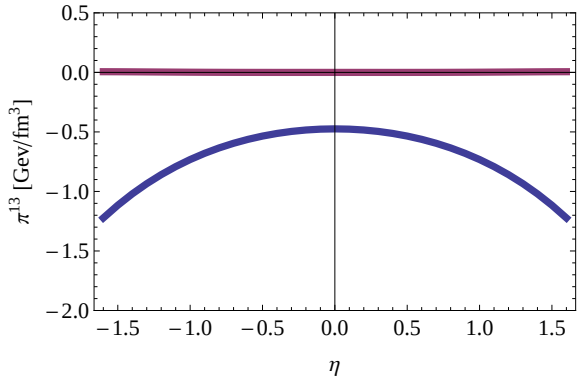

Figure 7.4: The shear stress π^{13} averaged over transverse coordinates as a function of η at thermalization time $\tau_{th} = 0.2$ fm (blue line) and at 0.8 fm (red line) after viscous hydrodynamic evolution.

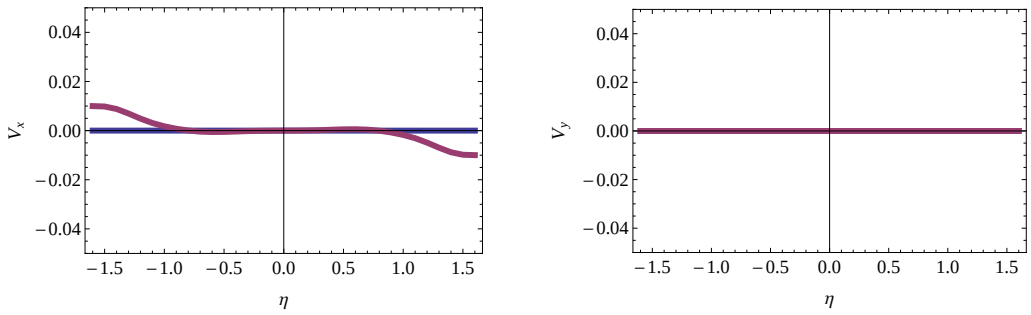

Figure 7.5: Left: The fluid velocity v_x averaged over transverse coordinates as a function of η at thermalization time $\tau_{th} = 0.2$ fm (blue line) and at 0.8 fm (red line) after viscous hydrodynamic evolution. Right: The fluid velocity v_y averaged over transverse coordinates at thermalization time $\tau_{th} = 0.2$ fm (blue line) and at 0.8 fm (red line) after viscous hydrodynamic evolution.

8. CONCLUSIONS AND REMARKS

The quest for understanding QGP is a challenging task. Significant achievements have been made since the launch of RHIC more than a decade ago. Aided by the recent run of LHC, we have reasons to believe that we will pin down properties of QGP at much more accurate precision in the near future. There are two questions that are of particular interest to nuclear physicists right now. First, is Color Glass Condensate the correct initial stage of heavy ion collision? Second, how perfect is the QGP fluid and what is the equation of state? Progress on these questions depends largely on improving our knowledge of the initial conditions of QGP. The research conducted in this dissertation can help us address these two questions.

We have generalized the McLerran-Venugopalan Model to accommodate transverse dynamics. The infrared safety of the color class description of an inhomogeneous nucleus is proved for the first time. With our generalization, color glass dynamics and long-distance dynamics, which is not described by CGC can be safely separated. The first (3+1)D solution of the glasma field including transverse flow is presented in this dissertation. Analytic expressions for event-averaged quantities have been provided as well as a code to produce event-by-event results. We also proposed a procedure of matching the glasma energy momentum tensor to viscous hydrodynamic to obtaining corresponding initial conditions.

The generalized McLerran-Venugopalan Model (MVTD) makes unique predictions for transverse flow of the glasma which have been overlooked in simple boost-invariant MV implementations. We find a rapidity-odd flow of energy. After matching to viscous hydrodynamics, the rapidity-odd flow of glasma will eventually translate into a directed flow of particles which is odd in momentum rapidity y, which

could contribute to directed flow v_1. Future phenomenological research using the (3+1)D viscous hydrodynamics will enable us to make predictions of directed flow of final particles from the CGC model. Moreover, the flow pattern for collision between asymmetric nuclei, e.g. Au+Cu collisions, becomes more involved. A systematic study of flow as a function of rapidity and different nuclear systems could help us find this characteristic feature of color glass. Such predictions, relating the momentum distribution of final particles to the energy momentum tensor of the glasma, if confirmed by experimental data, would be a unique signature for a CGC discovery claim.

Enormous efforts has been made to extract the shear viscosity of the QGP fluid [94]. Right now the largest uncertainty comes from initial conditions, which contribute almost 100% uncertainty [94]. The initial conditions at hand right now, usually set the initial velocities to 0, and set the initial shear stress tensor either to 0 or to its Navier-Stokes value. However the CGC predicts large initial transverse flow of the fireball [77, 58]. A theoretical calculation of the initial velocity and shear stress is critical to extract the viscosity of QGP correctly. In this dissertation, the first initial conditions for 3+1 viscous hydrodynamics with initial velocities and initial shear stress tensor is calculated from first principle CGC calculation.

REFERENCES

[1] D. J. Gross and F. Wilczek, Phys. Rev. Lett. **30**, 1343 (1973).

[2] H. D. Politzer, Phys. Rev. Lett. **30**, 1346 (1973).

[3] A. Bazavov, C. Bernard, C. DeTar, Steven Gottlieb, U.M. Heller *et al.*, Rev. Mod. Phys. **82**, 1349 (2010).

[4] K. Adcox *et al.* [PHENIX Collaboration], Nucl. Phys. A **757**, 184 (2005).

[5] J. Adams *et al.* [STAR Collaboration], Nucl. Phys. A **757**, 102 (2005).

[6] S. Borsanyi *et al.* [Wuppertal-Budapest Collaboration], JHEP **1009**, 073 (2010) [arXiv:1005.3508 [hep-lat]].

[7] A. Bazavov, T. Bhattacharya, M. Cheng, C. DeTar, H. T. Ding, S. Gottlieb, R. Gupta and P. Hegde *et al.*, Phys. Rev. D **85**, 054503 (2012) [arXiv:1111.1710 [hep-lat]].

[8] D. J. Gross, Nucl. Phys. Proc. Suppl. **74**, 426 (1999) [hep-th/9809060].

[9] M. Cheng, S. Ejiri, P. Hegde, F. Karsch, O. Kaczmarek, E. Laermann, R. D. Mawhinney and C. Miao *et al.*, Phys. Rev. D **81**, 054504 (2010) [arXiv:0911.2215 [hep-lat]], http://link.aps.org/abstract/PRD/v81/p054504.

[10] M. Luscher, Phys. Lett. B **428**, 342 (1998) [hep-lat/9802011].

[11] W. Weise, Prog. Part. Nucl. Phys. **67**, 299 (2012) [arXiv:1201.0950 [nucl-th]].

[12] E. O'Brien [PHENIX Collaboration], Nucl. Phys. A **904-905**, 264c (2013).

[13] K. Safarik [ALICE Collaboration], Nucl. Phys. A **904-905**, 27c (2013).

[14] B. Wosiek, ATL-PHYS-PROC-2012-224.

[15] G. Roland [CMS Collaboration], Nucl. Phys. A **904-905**, 43c (2013).

[16] N. Armesto, N. Borghini, S. Jeon, U. A. Wiedemann, S. Abreu, V. Akkelin, J. Alam and J. L. Albacete *et al.*, J. Phys. G **35**, 054001 (2008) [arXiv:0711.0974 [hep-ph]].

[17] P. Braun-Munzinger, K. Redlich and J. Stachel, In *Hwa, R.C. (ed.) et al.: Quark gluon plasma* 491-599 [nucl-th/0304013].

[18] J. D. Bjorken, FERMILAB-PUB-82-059-THY.

[19] M. Gyulassy, I. Vitev, X. -N. Wang and B. -W. Zhang, In *Hwa, R.C. (ed.) et al.: Quark gluon plasma* 123-191 [nucl-th/0302077].

[20] Y. Akiba [PHENIX Collaboration], Nucl. Phys. A **774**, 403 (2006) [nucl-ex/0510008].

[21] R. C. Hwa and C. B. Yang, Phys. Rev. C **67**, 034902 (2003) [nucl-th/0211010].

[22] R. J. Fries, B. Muller, C. Nonaka and S. A. Bass, Phys. Rev. Lett. **90**, 202303 (2003) [nucl-th/0301087].

[23] R. J. Fries, B. Muller, C. Nonaka and S. A. Bass, Phys. Rev. C **68**, 044902 (2003) [nucl-th/0306027].

[24] V. Greco, C. M. Ko and P. Levai, Phys. Rev. Lett. **90**, 202302 (2003) [nucl-th/0301093].

[25] V. Greco, C. M. Ko and P. Levai, Phys. Rev. C **68**, 034904 (2003) [nucl-th/0305024].

[26] K. Adcox *et al.* [PHENIX Collaboration], Phys. Rev. Lett. **88**, 242301 (2002) [nucl-ex/0112006].

[27] C. Adler *et al.* [STAR Collaboration], Phys. Rev. Lett. **86**, 4778 (2001) [Erratum-ibid. **90**, 119903 (2003)] [nucl-ex/0104022].

[28] R. A. Lacey and A. Taranenko, PoS CFRNC **2006**, 021 (2006) [nucl-ex/0610029].

[29] C. Gale and K. L. Haglin, In *Hwa, R.C. (ed.) et al.: Quark gluon plasma* 364-429 [hep-ph/0306098].

[30] T. Matsui and H. Satz, Phys. Lett. B **178**, 416 (1986).

[31] A. Bazavov, P. Petreczky and A. Velytsky, arXiv:0904.1748 [hep-ph].

[32] R. Rapp and H. van Hees, R. C. Hwa, X.-N. Wang (Ed.) Quark Gluon Plasma 4, World Scientific, 111 (2010) [arXiv:0903.1096 [hep-ph]].

[33] E. Iancu, arXiv:1205.0579 [hep-ph].

[34] E. Iancu, A. Leonidov and L. McLerran, hep-ph/0202270.

[35] A. H. Mueller and A. I. Shoshi, Nucl. Phys. B **692**, 175 (2004) [hep-ph/0402193].

[36] L. D. McLerran and R. Venugopalan, Phys. Rev. D **49**, 2233 (1994) [arXiv:hep-ph/9309289].

[37] L. D. McLerran and R. Venugopalan, Phys. Rev. D **49**, 3352 (1994) [arXiv:hep-ph/9311205].

[38] J. Jalilian-Marian and Y. V. Kovchegov, Prog. Part. Nucl. Phys. **56**, 104 (2006) [hep-ph/0505052].

[39] F. Gelis, E. Iancu, J. Jalilian-Marian and R. Venugopalan, Ann. Rev. Nucl. Part. Sci. **60**, 463 (2010) [arXiv:1002.0333 [hep-ph]].

[40] U. W. Heinz and P. F. Kolb, Nucl. Phys. A **702**, 269 (2002) [hep-ph/0111075].

[41] D. Kharzeev, E. Levin and K. Tuchin, Phys. Rev. C **75**, 044903 (2007) [hep-ph/0602063].

[42] C. Manuel and S. Mrowczynski, Phys. Rev. D **68**, 094010 (2003) [hep-ph/0306209].

[43] A. Kurkela and G. D. Moore, JHEP **1112**, 044 (2011) [arXiv:1107.5050 [hep-ph]].

[44] S. A. Bass, M. Belkacem, M. Bleicher, M. Brandstetter, L. Bravina, C. Ernst, L. Gerland and M. Hofmann *et al.*, Prog. Part. Nucl. Phys. **41** (1998) 255 [Prog. Part. Nucl. Phys. **41** (1998) 225] [nucl-th/9803035].

[45] L. D. Landau, Izv. Akad. Nauk Ser. Fiz. **17** (1953) 51.

[46] J. D. Bjorken, Phys. Rev. D **27**, 140 (1983).

[47] P. F. Kolb and U. W. Heinz, in *Quark Gluon Plasma 3*, ed. R. C. Hwa et al., World Scientific (2003), preprint nucl-th/0305084.

[48] R. J. Fries and C. Nonaka, Prog. Part. Nucl. Phys. **66**, 607 (2011)

[49] I. Muller, Z. Phys. **198**, 329 (1967).

[50] W. Israel, Annals Phys. **100**, 310 (1976).

[51] A. Muronga, Phys. Rev. C **69**, 034903 (2004) [nucl-th/0309055].

[52] R. Baier, P. Romatschke, D. T. Son, A. O. Starinets and M. A. Stephanov, JHEP **0804**, 100 (2008) [arXiv:0712.2451 [hep-th]].

[53] P. Romatschke, Int. J. Mod. Phys. E **19**, 1 (2010) [arXiv:0902.3663 [hep-ph]].

[54] D. A. Teaney, arXiv:0905.2433 [nucl-th].

[55] M. L. Miller, K. Reygers, S. J. Sanders and P. Steinberg, Ann. Rev. Nucl. Part. Sci. **57**, 205 (2007) [nucl-ex/0701025].

[56] D. Kharzeev, E. Levin and M. Nardi, Nucl. Phys. A **730**, 448 (2004) [Erratum-ibid. A **743**, 329 (2004)] [hep-ph/0212316].

[57] D. Kharzeev and M. Nardi, Phys. Lett. B **507**, 121 (2001) [nucl-th/0012025].

[58] B. Schenke, P. Tribedy and R. Venugopalan, Phys. Rev. Lett. **108**, 252301 (2012)

[59] B. Schenke, P. Tribedy and R. Venugopalan, Phys. Rev. C **86**, 034908 (2012) [arXiv:1206.6805 [hep-ph]].

[60] R. J. Fries, J. I. Kapusta and Y. Li, arXiv:nucl-th/0604054.

[61] R. J. Fries, J. I. Kapusta and Y. Li, unpublished.

[62] A. Kovner, L. D. McLerran and H. Weigert, Phys. Rev. D **52**, 3809 (1995); Phys. Rev. D **52**, 6231 (1995).

[63] T. Lappi, Phys. Lett. B **643**, 11 (2006).

[64] A. Krasnitz and R. Venugopalan, Phys. Rev. Lett. **86**, 1717 (2001) [arXiv:hep-ph/0007108].

[65] T. Lappi, Phys. Rev. C **67**, 054903 (2003) [arXiv:hep-ph/0303076].

[66] A. Krasnitz, Y. Nara and R. Venugopalan, Nucl. Phys. A **727**, 427 (2003) [arXiv:hep-ph/0305112].

[67] R. J. Fries, J. I. Kapusta and Y. Li, Nucl. Phys. A **774**, 861 (2006) [arXiv:hep-ph/0511101].

[68] R. J. Fries, B. Muller and A. Schafer, Phys. Rev. C **79**, 034904 (2009) [arXiv:0807.1093 [nucl-th]].

[69] R. J. Fries, T. Kunihiro, B. Muller, A. Ohnishi and A. Schafer, Nucl. Phys. A **830**, 519C (2009) [arXiv:0906.5293 [nucl-th]].

[70] T. Lappi and L. McLerran, Nucl. Phys. A **772**, 200 (2006)

[71] J. S. Schwinger, Phys. Rev. **82**, 664 (1951).

[72] D. E. Kharzeev, Y. V. Kovchegov and E. Levin, Nucl. Phys. A **699**, 745 (2002) [hep-ph/0106248].

[73] D. Kharzeev, A. Krasnitz and R. Venugopalan, Phys. Lett. B **545**, 298 (2002) [hep-ph/0109253].

[74] G. Chen, R. J. Fries, J. I. Kapusta and Y. Li, in preparation

[75] I. G. Bearden *et al.* [BRAHMS Collaboration], Phys. Rev. Lett. **93**, 102301 (2004).

[76] G. Chen and R. J. Fries, Journal of Physics: Conference Series, (2013). arXiv:1212.4119 [nucl-th].

[77] G. Chen and R. J. Fries, Phys. Lett. B, **723**, 417, (2013).

[78] J. Jalilian-Marian, A. Kovner, L. D. McLerran and H. Weigert, Phys. Rev. D **55**, 5414 (1997).

[79] H. Fujii, K. Fukushima and Y. Hidaka, Phys. Rev. C **79**, 024909 (2009)

[80] K. Fukushima and Y. Hidaka, JHEP **0706**, 040 (2007) [arXiv:0704.2806 [hep-ph]].

[81] B. I. Abelev *et al.* [STAR Collaboration], Phys. Rev. Lett. **101**, 252301 (2008), http://link.aps.org/abstract/PRL/v101/p252301.

[82] J. Adams *et al.* [STAR Collaboration], Phys. Rev. C **73**, 034903 (2006)

[83] B. B. Back *et al.* [PHOBOS Collaboration], Phys. Rev. Lett. **97**, 012301 (2006) [nucl-ex/0511045].

[84] L. P. Csernai, V. K. Magas, H. Stocker and D. D. Strottman, Phys. Rev. C **84**, 024914 (2011)

[85] J. Gosset, J. I. Kapusta and G. D. Westfall, Phys. Rev. C **18**, 844 (1978)

[86] C. S. Lam and G. Mahlon, Phys. Rev. D **61**, 014005 (2000) [hep-ph/9907281].

[87] A. Krasnitz, Y. Nara and R. Venugopalan, Nucl. Phys. A **717**, 268 (2003) [hep-ph/0209269].

[88] R. Rodriguez, R. J. Fries and E. Ramirez, Phys. Lett. B **693**, 108 (2010) [arXiv:1005.3567 [nucl-th]].

[89] T. Lappi, Eur. Phys. J. C **55**, 285 (2008) [arXiv:0711.3039 [hep-ph]].

[90] J. G. F. Francis, The Computer Journal, 4, 265 (1961). J. G. F. Francis, The Computer Journal, 4, 332 (1961).

[91] S. Somanathan and R.J. Fries, in preparation.

[92] R. J. Fries, J. Phys. G **34**, S851 (2007) [nucl-th/0702026 [NUCL-TH]].

[93] B. Alver and G. Roland, Phys. Rev. C **81**, 054905 (2010) [Erratum-ibid. C **82**, 039903 (2010)] [arXiv:1003.0194 [nucl-th]].

[94] H. Song, Nucl. Phys. A904-905 **2013**, 114c (2013) [arXiv:1210.5778 [nucl-th]].

5Rev. Mod. Phys. **59**, 465 (1987).